Journal of Sound and Vibration 329 (2010) 3813–3834

Contents lists available at ScienceDirect

Journal of Sound and Vibration

journal homepage: www.elsevier.com/locate/jsvi

Nonlinear dynamics of harmonically excited circular cylindrical shells containing fluid flow

K. Karagiozis, M. Amabili *, M.P. Païdoussis

Department of Mechanical Engineering, McGill University, 817 Sherbrooke Street West, Montreal, Québec, Canada H3A 2K6

ARTICLE INFO

Article history:
Received 27 August 2009
Received in revised form
11 February 2010
Accepted 16 March 2010
Handling Editor: M.P. Cartmell
Available online 24 April 2010

ABSTRACT

In the present study, the geometrically nonlinear vibrations of circular cylindrical shells, subjected to internal fluid flow and to a radial harmonic excitation in the spectral neighbourhood of one of the lowest frequency modes, are investigated for different flow velocities. The shell is modelled by Donnell's nonlinear shell theory, retaining in-plane inertia and geometric imperfections; the fluid is modelled as a potential flow with the addition of unsteady viscous terms obtained by using the time-averaged Navier–Stokes equations. A harmonic concentrated force is applied at mid-length of the shell, acting in the radial direction. The shell is considered to be immersed in an external confined quiescent liquid and to contain a fluid flow, in order to reproduce conditions in previous water-tunnel experiments. For the same reason, complex boundary conditions are applied at the shell ends simulating conditions intermediate between clamped and simply supported ends. Numerical results obtained by using pseudo-arclength continuation methods and bifurcation analysis show the nonlinear response at different flow velocities for (i) a fixed excitation amplitude and variable excitation frequency, and (ii) fixed excitation frequency by varying the excitation amplitude. Bifurcation diagrams of Poincaré maps obtained from direct time integration are presented, as well as the maximum Lyapunov exponent, in order to classify the system dynamics. In particular, periodic, quasi-periodic, sub-harmonic and chaotic responses have been detected. The full spectrum of the Lyapunov exponents and the Lyapunov dimension have been calculated for the chaotic response; they reveal the occurrence of large-dimension hyperchaos.

1. Introduction

Shells containing flowing fluids may be found in many engineering and biomechanical systems. Most of these systems are made of thin circular cylindrical shells designed for weight economy and cost management. However, for thin shells, vibrations are a major problem due to excitations of many kinds, including flow-induced excitations. In most previous studies, linear shell theory has been used to describe the oscillation of thin shells coupled to a flowing fluid, which is accurate only for vibration amplitudes significantly smaller than the shell thickness.

One of the first complete studies on the dynamics of shells conveying fluid was by Païdoussis and Denise [1] for both clamped and cantilevered shells subjected to axial flow; a travelling-wave type solution was utilized, nevertheless satisfying the pertinent boundary conditions, along with a separation of variables method to solve the boundary value

---

* Corresponding author. Tel.: +1 514 398 3068; fax: +1 514 398 7365.
E-mail address: marco.amabili@mcgill.ca (M. Amabili).
URL: http://people.mcgill.ca/marco.amabili/ (M. Amabili).

0022-460X/$ - see front matter © 2010 Elsevier Ltd. All rights reserved.
doi:10.1016/j.jsv.2010.03.022

problem for linear fluid–structure interaction. Weaver and Unny [2], on the other hand, investigated the stability of simply supported shells by means of the Fourier transform method. Païdoussis et al. [3] extended this method to coaxial cylindrical shells. Systematic research in this area has been conducted by Païdoussis and it is synthesized in his monograph [4]. Horáček and Zolotarev [5] investigated the effect of different boundary conditions at the shell ends. The effects of boundary conditions and fluid viscosity were investigated further by Amabili and Garziera [6,7]; the effect of the boundary conditions and shell tapering were studied by Ugurlu and Ergin [8]. Anisotropic shells coupled to flowing fluid were considered by Toorani and Lakis [9–11]. Finite element models to study linear vibration of cylindrical shells conveying fluid were developed by Zhang et al. [12,13]. In the literature discussed here, not only the shell stability but also the dependence of the natural frequencies of the shell on the flow velocity has been investigated.

The literature related to nonlinear studies of shells coupled to flowing fluid is not large. Selmane and Lakis [14] studied the large amplitude vibration of shells with flow. They considered the nonlinear free vibrations of open and closed circular cylindrical shells with fluid flow by using a hybrid finite element method. The formulation is based on the nonlinear Sanders-Koiter shell theory, so that structural nonlinearities are taken into account. Results have been obtained for free nonlinear vibrations of an open circular cylindrical shell with flowing fluid.

In a series of papers, Amabili, Pellicano and Païdoussis [15–18] systematically studied the nonlinear dynamics, stability and large-amplitude vibrations of simply supported, circular cylindrical shells, with quiescent or flowing fluid. In the last paper of the series [18], they investigated the nonlinear vibrations of a simply supported, circular cylindrical shell containing flowing fluid and subjected to harmonic excitation, by using a model with seven degrees of freedom. Potential flow theory and Donnell's nonlinear shallow-shell theory were used to model the flow and the shell, respectively.

The stability of circular cylindrical shells conveying or immersed in flowing fluid was studied by Amabili, Pellicano and Païdoussis [15,19,20]. For the first time it was found that circular cylindrical shells become unstable through a strongly subcritical pitchfork bifurcation; this means that shells can diverge statically (buckle) due to fluid flow, much before the stability threshold predicted by linear stability calculations is reached. Karagiozis et al. [21,22] confirmed these findings by comparing numerical and experimental results; experiments in a water tunnel were appositely performed in order to validate the theory. The same findings were confirmed by using more accurate shell theories by Amabili et al. [23]; the effect of geometric imperfections was also investigated.

Computer programs based on the finite-element method (FEM) have been used to model arterial and capillary vessels (modelled with shell elements) conveying blood flow (see e.g. Bathe and Kamm [24]). However, FEM simulations of nonlinear dynamics and the stability of similar problems are still far from reliable.

The literature on nonlinear vibrations of circular cylindrical shells not coupled to flow is quite abundant; it has been reviewed by Amabili and Païdoussis [25]. An introduction and state-of-the-art is given in the monograph by Amabili [26]; here, only a few studies are reviewed, specifically those related to the present study. Amabili [27] investigated the effect of geometric imperfections on nonlinear vibrations of circular cylindrical shells containing still water and compared calculations and experiments, thus validating the theory. More accurate shell theories have been used by Amabili [28] to study the same problem. Results show that, for water-filled shells, the Donnell's nonlinear shell theory gives very accurate results for thin shells, provided the in-plane inertia is taken into account. Chaotic vibrations of spherical shells were studied by Soliman and Gonçalves [29], while complex nonlinear dynamics of circular cylindrical shells was investigated by Amabili et al. [30].

In the present study, the geometrically nonlinear vibrations of circular cylindrical shells, subjected to internal fluid flow and to a radial harmonic excitation in the spectral neighbourhood of one of the lowest frequency modes, are investigated for different flow velocities. The shell is modelled by using the form of Donnell's nonlinear shell theory retaining in-plane inertia; the fluid is modelled as a potential flow, yet taking into account additional unsteady viscous terms obtained via the time-averaged Navier–Stokes equations. A harmonic concentrated force applied at mid-length of the shell and acting in radial direction is assumed. The shell is considered to be immersed in a confined external quiescent liquid and to contain a fluid flow, in order to be able to compare with previous water-tunnel experiments [22,23]. For the same reason, complex boundary conditions are applied at both ends of the shell; modelling conditions ranging from simply supported to clamped ends. Numerical results obtained by using the pseudo-arclength continuation method and bifurcation analysis give the nonlinear response at different flow velocities for (i) fixed excitation amplitude and varying excitation frequency, and (ii) fixed excitation frequency and varying excitation amplitude. Bifurcation diagrams of Poincaré maps obtained from direct time integration are presented, as well as the maximum Lyapunov exponent, in order to classify the system dynamics. As will be seen, periodic, quasi-periodic, sub-harmonic and chaotic responses have been detected. The full spectrum of the Lyapunov exponents and the Lyapunov dimension have been calculated for the chaotic response, demonstrating the occurrence of hyperchaos. The present study extends the model previously developed by the same authors [23] for studying the nonlinear behaviour of the system subjected to external excitation.

2. Shell and fluid–structure interaction models

Fig. 1 shows the system under consideration. It consists of a thin circular cylindrical shell of length L, mean radius R, and thickness h, such that $h/R \ll 1$. The origin of the cylindrical coordinate system,$(O; x, r, \theta)$, is positioned at the centre of one end of the shell. The shell is assumed to be of homogeneous, isotropic elastic material of Young's modulus E and Poisson's

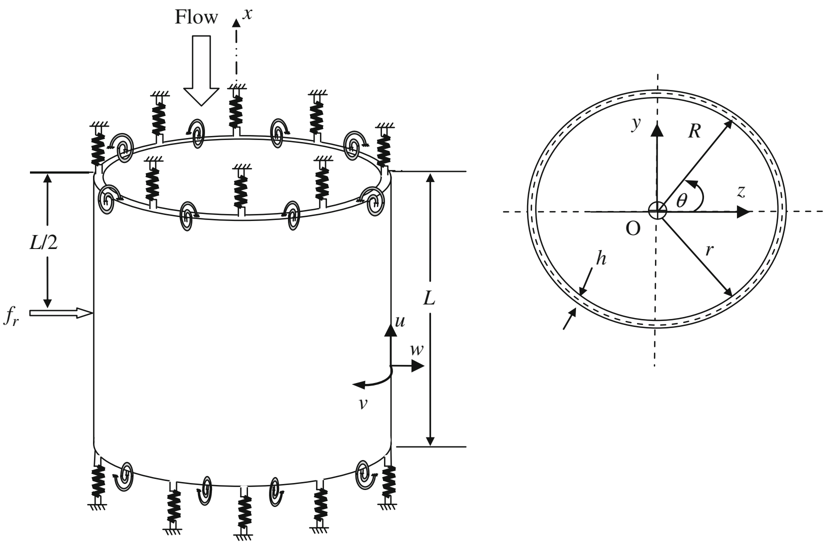

Fig. 1. Shell geometry, boundary conditions (translational and rotational springs) and coordinate system.

ratio ν. The displacements of the shell middle surface are denoted by u, v and w, in the axial, circumferential and radial directions, respectively; w is taken positive outward. Only radial initial imperfections are considered in this study neglecting locked-in initial stresses. These geometrical imperfections are directly associated with zero initial tension and they are represented by an inward displacement w_0. The shell contains an internally flowing fluid, is immersed in a quiescent external fluid, and is subjected to an external harmonic excitation force, as indicated in Fig. 1.

In the following sub-sections, the model is synthesized; some of the details of the basic model—without force excitation—may be found in [23].

2.1. Structural model

The following boundary conditions are imposed at the shell ends (see Fig. 1):

$$v = w = w_0 = 0, \quad \text{at } x = 0, L, \tag{1a–c}$$

$$N_x = -k_a u, \quad \text{at } x = 0, L, \tag{1d}$$

$$M_x = -k_r(\partial w/\partial x), \quad \text{at } x = 0, L, \tag{1e}$$

where N_x is the axial stress resultant per unit length, M_x is the bending moment per unit length, k_a is the stiffness per unit length of the elastic, distributed axial springs at x=0 and L and k_r is the stiffness per unit length of the elastic, distributed rotational springs at x=0 and L. Moreover, u, v and w must be continuous in θ. The boundary conditions (1a,b) restrain the radial and circumferential shell displacements at the two edges. Eq. (1d) gives the elastic axial constraint at the shell edges. Different values of the axial spring k_a are assumed for asymmetric (k_{a1}) and axisymmetric (k_{a2}) vibration modes in the numerical calculations in order to simulate experimental boundary conditions. Eq. (1e) represents an elastic rotational constraint at the shell edges. It gives any rotational constraint from zero moment (M_x=0, unconstrained rotation) to a perfectly rotationally clamped shell ($\partial w/\partial x = 0$, obtained as limit for $k_r \to \infty$), according to the value of k_r. For not very short thin shells, the axial spring k_a plays a much larger role than the rotational spring k_r, as indicated in [31].

The displacements u, v and w can be expanded to facilitate discretization of the equations by using the following expressions, which identically satisfy boundary conditions (1a,b):

$$u(x,\theta,t) = \sum_{m=1}^{5} [u_{m,n,c}(t)\cos(n\theta) + u_{m,n,s}(t)\sin(n\theta)]\cos(\lambda_m x) + \sum_{m=1}^{3} u_{m,2n,c}(t)\cos(2n\theta)\cos(\lambda_m x) + \sum_{m=1}^{4} u_{2m-1,0}(t)\cos(\lambda_{2m-1} x), \tag{2a}$$

$$v(x,\theta,t) = \sum_{m=1}^{5} [v_{m,n,c}(t)\sin(n\theta) + v_{m,j,s}(t)\cos(n\theta)]\sin(\lambda_m x) + \sum_{m=1}^{4} v_{m,2n,c}(t)\sin(2n\theta)\sin(\lambda_m x), \tag{2b}$$

$$w(x,\theta,t) = \sum_{m=1}^{3} [w_{m,n,c}(t)\cos(n\theta) + w_{m,n,s}(t)\sin(n\theta)]\sin(\lambda_m x) + \sum_{m=1}^{4} w_{2m-1,0}(t)\sin(\lambda_{2m-1} x), \tag{2c}$$

where n is the circumferential wavenumber, m is the number of longitudinal half-waves, $\lambda_m = m\pi/L$, and t is the time; $u_{m,n}(t)$, $v_{m,n}(t)$ and $w_{m,n}(t)$ are the generalized coordinates, which are unknown functions of t; the additional subscript c or s indicates if the generalized coordinate is associated to a driven mode (i.e. a mode directly excited by the external excitation) or a companion mode (a mode indirectly excited, contributing only to the system response due to nonlinear coupling); no additional subscript is used for axisymmetric terms. Eqs. (2a–c) have been obtained for an excitation frequency close to that of mode (n, m); therefore, generalized coordinates with a different number of circumferential waves from those in Eqs. (2a–c) can be neglected. It must be observed that in the nonlinear case a coupling among different n arises (e.g. in Eqs. 2(a) and 2(b)), and decoupling in the n variable is not automatic.

The number of terms in the longitudinal and circumferential direction in Eqs. (2a–c) must be selected with care in order to obtain the required accuracy and acceptable dimension of the nonlinear problem. More terms are necessary for in-plane than for radial displacements. Torsional axisymmetric terms are not necessary since torsional axisymmetric modes are uncoupled from axial and radial axisymmetric modes. In Eqs. (2), terms with an even number of longitudinal waves, i.e. m=2, are kept into the expansion since they are coupled to the odd modes in the presence of flowing fluid also in case of small amplitude (i.e. linear) vibrations. In fact a shell conveying fluid exhibits complex modes; as a consequence, all points on the shell do not move in phase. Results on the stability of a shell conveying water with the same boundary conditions as considered here show a uniform convergence of the solution from two to six longitudinal modes are included [23]. The total number of degrees of freedom used in the present model is 42.

Imperfections are expanded in the following Fourier series:

$$w_0(x,\theta,t) = \sum_{m=1}^{\hat{M}} \sum_{j=0}^{\hat{N}} [A_{m,j}\cos(j\theta) + B_{m,j}\sin(j\theta)]\sin(m\pi x/L). \tag{2d}$$

The kinetic energy of the shell is given by

$$T_S = \frac{1}{2}\rho_S h \int_0^{2\pi} \int_0^L (\dot{u}^2 + \dot{v}^2 + \dot{w}^2)\,\mathrm{d}x R\,\mathrm{d}\theta, \tag{3}$$

where ρ_S is the mass density of the shell. The potential energy of the shell U_S is made up of two contributions: the elastic strain energy U_{shell} of the circular cylindrical shell and the potential energy U_{spring} stored by the axial and rotational distributed springs at the shell ends; therefore,

$$U_S = U_{\text{shell}} + U_{\text{spring}}. \tag{4}$$

The elastic strain energy U_{shell} of a circular cylindrical shell is given by [26],

$$U_{\text{shell}} = \frac{1}{2}\int_0^{2\pi} \int_0^L \int_{-h/2}^{h/2} (\sigma_x \varepsilon_x + \sigma_\theta \varepsilon_\theta + \tau_{x\theta}\gamma_{x\theta})\,\mathrm{d}x R(1+z/R)\,\mathrm{d}\theta\,\mathrm{d}z, \tag{5}$$

where h is the shell thickness, R the shell middle radius, L the shell length, and the stresses σ_x, σ_θ and $\tau_{x\theta}$ are related to the strains ε_x, ε_θ and $\varepsilon_{x\theta}$ for homogeneous isotropic material (σ_z=0, case of plane stress) [26]. Donnell's nonlinear shell theory [26] retaining in-plane inertia is used in order to evaluate Eqs. (3)–(5). The model has been developed and validated by Amabili et al. [23].

The potential energy stored by the axial and rotational springs at the shell ends is given by

$$U_{\text{spring}} = \frac{1}{2}\int_0^{2\pi} \left\{ k_a[(u_a)_{x=0}]^2 + k_a[(u_a)_{x=L}]^2 + k_r\left[\left(\frac{\partial w}{\partial x}\right)_{x=0}\right]^2 + k_r\left[\left(\frac{\partial w}{\partial x}\right)_{x=L}\right]^2 \right\}\mathrm{d}\theta, \tag{6}$$

where u_a is the axial displacement given by Eq. (2a) without the axisymmetric terms $u_{m,0}(t)$.

2.2. *Fluid–structure interaction for inviscid fluid*

The contained flowing fluid and the external quiescent fluid are assumed to be incompressible and inviscid and the flow isentropic and irrotational, so that potential flow theory can be used to describe fluid motion. Potential flow has been verified to give accurate results to study stability and dynamics of shells conveying fully developed water and air flow (in the incompressible regime). Nonlinear effects in the dynamic pressure and in the boundary conditions at the fluid–structure interface are neglected; accounting for these nonlinear effects has been shown to give negligible effects [32–34]. The shell prestress due to the fluid weight is also neglected, which is reasonable for shells that are not extremely thin. The fluid motion is described by the velocity potential Φ, which satisfies the Laplace equation. A very long shell periodically supported at L intervals is assumed in order to use the separation of variables method.

The irrotationality property is the condition for existence of a scalar potential function Ψ, from which the velocity may be written as

$$V = \nabla\Psi. \tag{7}$$

By using the Green's theorem, the total energy E_F associated with the flow can conveniently be divided into three terms with different contributions of time functions and their derivatives:

$$E_F = T_F + E_G - V_F; \tag{8}$$

the first and second of the three terms on the right-hand side can be identified as the kinetic and gyroscopic energies, respectively; an opposite sign is introduced for the potential energy V_F, for convenience.

2.3. Fluid viscosity effect

In order to improve the potential flow model introduced in Section 2.2, the effect of steady fluid viscosity is added to the model. The time-mean Navier–Stokes equations [23,35], are employed to calculate the fluid steady viscous effects assuming that the flow is fully turbulent. The unsteady viscous forces [4] are neglected in this investigation. There are two steady viscous effects: (i) a pressure drop along the shell length, so that a zero pressure differential across the shell surface is defined at the shell mid-length, and (ii) axial friction forces distributed on the shell internal surface.

2.4. Generalized forces

In this analysis, the shell is subjected not only to flowing fluid but also to an external harmonic force excitation of frequency ω active only in the radial direction, as indicated in Fig. 1. The external localized (point) force on the shell surface is directed inwards and is applied at a point $(\tilde{x},\tilde{\theta})$. The excitation force in the radial direction has the following general form:

$$f_r=\tilde{f}\,\delta(R\theta-R\tilde{\theta})\delta(x-\tilde{x})cos(\omega t), \tag{9}$$

where δ is the Dirac delta function, and $\tilde{f}$ is the magnitude of the point force. It is important to note that in the present analysis the driving frequency (excitation frequency) is chosen to have values close to the natural frequency of the lowest modes of the shell. The low-frequency modes are associated with predominantly radial motion and are identified by the pair (m, n), where m is the number of axial half-waves and n is the number of circumferential waves. The external force in Eq. (9) can be used to describe the excitation provided by an electrodynamic exciter (shaker), for instance.

The virtual work W done by the external force is written as

$$W=\int_0^{2\pi}\int_0^{L}(f_x u+f_\theta v+f_r w)\,\mathrm{d}xR\,\mathrm{d}\theta, \tag{10}$$

where f_x, f_θ, and f_r are the distributed forces per unit area acting in the axial, circumferential and radial directions, respectively. In our study it is assumed that $f_x=f_\theta=0$. Therefore, Eq. (10) can be rewritten as

$$W=\tilde{f}\,\cos(\omega t)(w)_{x=L/2,\ \theta=0}. \tag{11}$$

Damping is considered to arise strictly within the shell material. It is assumed to be of the viscous type and is taken into account by using Rayleigh's dissipation function

$$F=\frac{1}{2}c\int_0^{2\pi}\int_0^{L}(\dot{u}^2+\dot{v}^2+\dot{w}^2)\,\mathrm{d}xR\,\mathrm{d}\theta, \tag{12}$$

where c has a different value for each term of the mode expansion. Although damping in the fluid is neglected, its overall effect may be approximated by appropriately augmenting c. In fact, in the calculations, modal damping is utilized, which can represent the total damping in the system.

The generalized forces Q_j are obtained by differentiation of the Rayleigh's dissipation function and of the virtual work W done by external forces:

$$Q_j=-\frac{\partial F}{\partial \dot{q}_j}+\frac{\partial W}{\partial q_j}, \tag{13}$$

where $\partial F/\partial \dot{q}_j=c_j\dot{q}_j$.

2.5. Lagrange equations of motion

The following notation is introduced:

$$\mathbf{q}=\{u_{m,n,c},u_{m,n,s},v_{m,n,c},v_{m,n,s},w_{m,n,c},w_{m,n,s}\}^{\mathrm{T}},\quad m=1,\dots,M \text{ and } n=0,\dots,N. \tag{14}$$

The generic element of the time-dependent vector $\mathbf{q}$ is referred to as q_j. The dimension of $\mathbf{q}$ is $\overline{N}=42$, which is the number of degrees of freedom used in the mode expansion.

In the present case, the Lagrange equations of motion are rewritten as

$$\frac{\mathrm{d}}{\mathrm{d}t}\left[\frac{\partial(T_S+T_F+E_G)}{\partial \dot{q}_j}\right]-\frac{\partial(T_S+T_F+E_G)}{\partial q_j}+\frac{\partial(U_S+V_F)}{\partial q_j}=Q_j,\quad j=1,\dots,\overline{N}, \tag{15}$$

where T_S and T_F are the kinetic energy of the shell and the fluid, respectively, U_S and V_F are the potential energy of the shell and the fluid, respectively, E_G is the gyroscopic energy, $\partial T_S/\partial q_j=0$ and $\partial T_F/\partial q_j=0$.

3. Solution method

The 42 second-order nonlinear ordinary differential equations are divided by the modal mass and further simplified to 84 first-order differential equations using a dummy variable y_j. The final set of ODEs is given in the following expressions:

$$\begin{cases} \dot{q}_j = y_j \\ \dot{y}_j = -2\zeta_j\omega_j y_j - \sum_{i=1}^{\overline{N}} z_{j,i}q_i - \sum_{i=1}^{\overline{N}}\sum_{k=1}^{\overline{N}} z_{j,i,k}q_iq_k - \sum_{i=1}^{\overline{N}}\sum_{k=1}^{\overline{N}}\sum_{l=1}^{\overline{N}} z_{j,i,k,l}q_iq_kq_l + \tilde{f}_j\cos(\omega t), \end{cases} \quad \text{for } j = 1,\ldots,\overline{N}, \tag{16}$$

where $z_{j,i}$ are the coefficients associated with the linear stiffness terms (transformed in the elimination of the mass from the equations), $z_{j,i,k}$ are the coefficients associated with quadratic stiffness terms and $z_{j,i,k,l}$ are the coefficients associated with cubic stiffness terms; ζ_j is the modal damping ratio, which can be related to the damping coefficient c introduced in Eq. (12) and ω_j is the natural frequency of the jth mode. The force amplitude $\tilde{f}_j$ takes different values according to Eq. (11) and is equal to 0 for any generalized coordinate different than $w_{m,n,c}$.

Once nondimensionalized, the resulting ODEs are studied via two numerical schemes. The first employs a continuation method to follow both the stable and unstable solutions. The software AUTO [36] is capable of continuation of the solution, bifurcation analysis and branch switching by using the pseudo-arclength continuation and collocation methods.

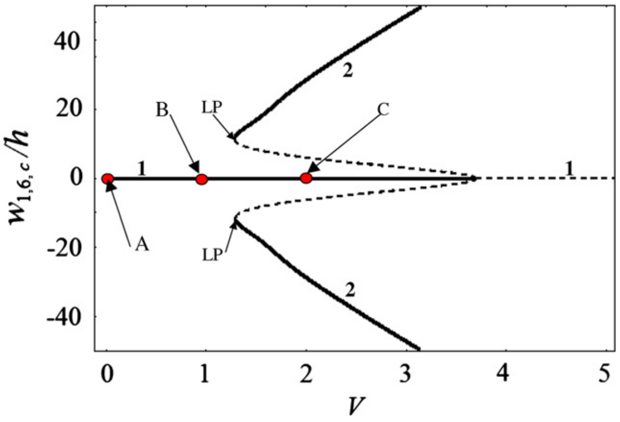

Fig. 2. Bifurcation diagram of the non-dimensional amplitude of the first driven mode $w_{1,6,c}/h$ versus the non-dimensional flow velocity V of a clamped aluminium shell with internal water flow: ———, stable solution branches; – – – – –, unstable solution branches. A, B and C are points of interest at V=0, 1 and 2, respectively, and LP are the limit points of the solution branches.

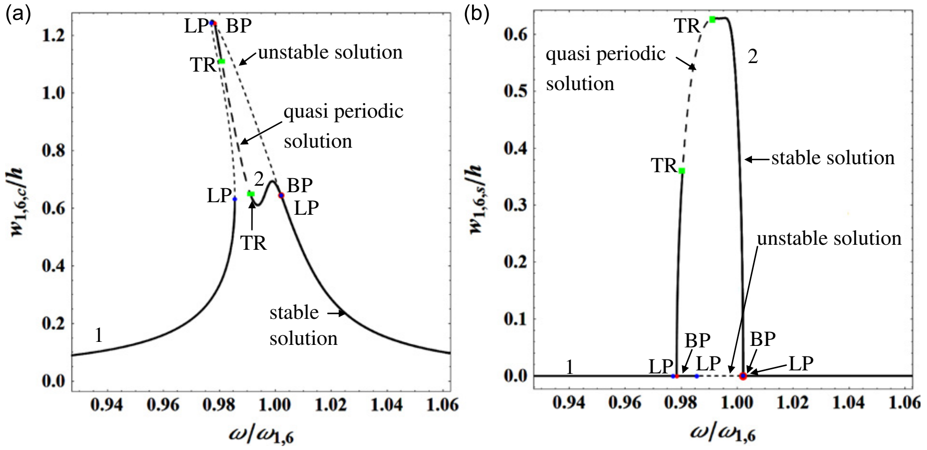

Fig. 3. The amplitude–frequency response of the driven and companions modes for case A, using Donnell's theory with modal structural damping equal to 0.005 and $\tilde{f} = 0.0165$ N: ———, stable response; – – – – –, unstable response. (a) Amplitude of the driven mode; (b) amplitude of the companion mode. TR corresponds to torus bifurcation points, LP denotes a limit point and BP represents the bifurcation points.

In particular, for this study the shell response under harmonic excitation has been investigated in two steps: (i) first, the excitation frequency has been fixed far enough from resonance, and the magnitude of the excitation has been used as the bifurcation parameter; then, the solution is found, starting with zero initial conditions until the desired magnitude for the excitation is reached; (ii) in the second step the shell has been excited at the maximum force level and the shell amplitude is computed, using the excitation frequency now as the bifurcation parameter.

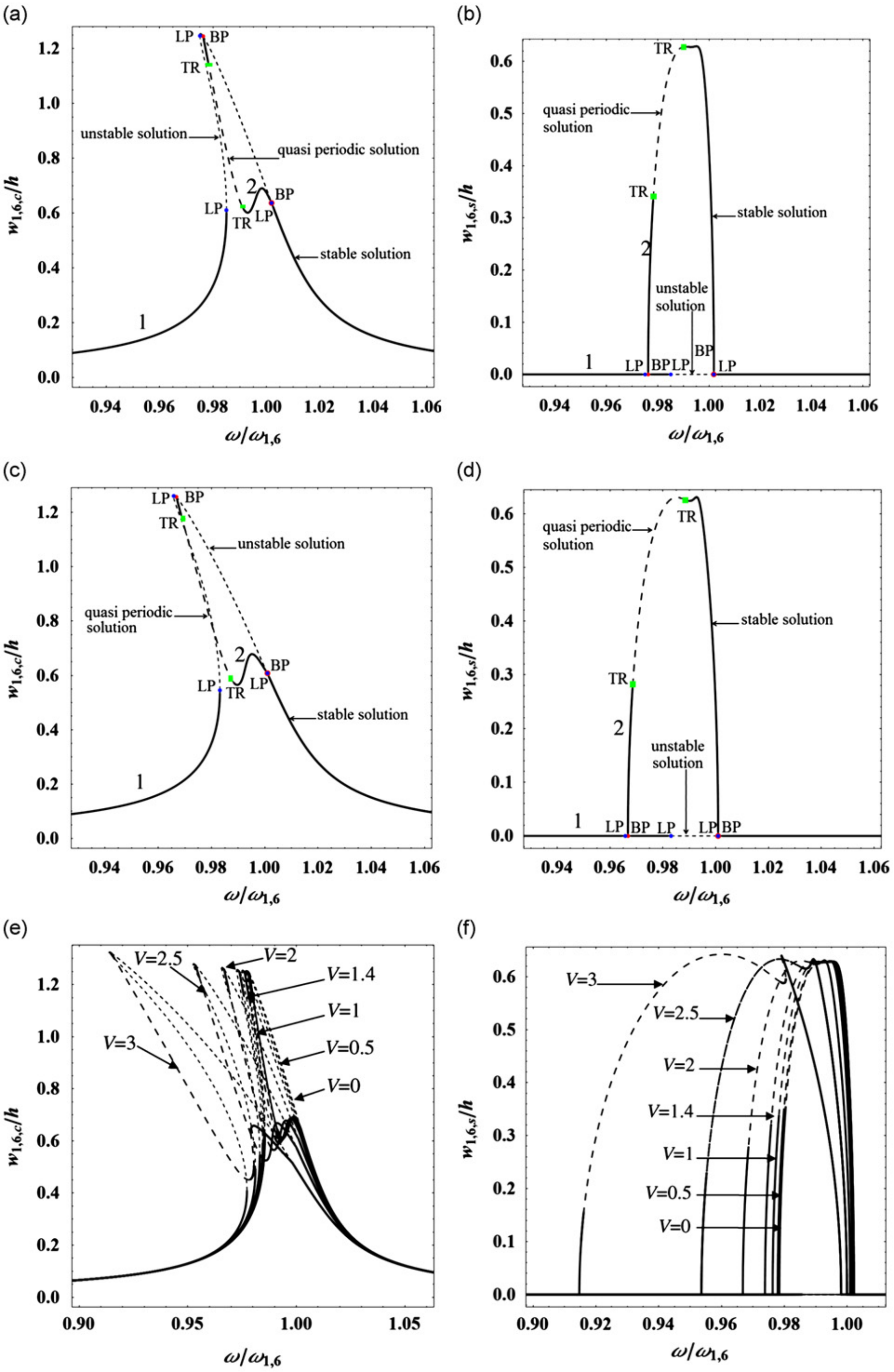

Fig. 4. The amplitude–frequency response of the driven and companions modes for different velocity cases for $\tilde{f} = 0.0165$ N: ——, stable response; – – – – –, unstable response. (a) Driven mode amplitude for case B; (b) companion mode amplitude for case B; (c) driven mode response for case C; (d) companion mode response for case C; (e) composite of driven modes for different velocity cases; (f) composite of companion modes for different velocity cases.

The second numerical method involves direct time integration of the equations of motion. In this study, the DIVPAG numerical routine from the Fortran IMSL library is used to perform the time integration. In particular, Gear's backward-differentiation-formula (BDF) is used to deal with the stiff nonlinear equations. The direct time integration was used to obtain the bifurcation diagrams and Poincaré maps for the non-stationary responses. Specifically, in this case, the maximum Lyapunov exponent was evaluated so as to identify regimes of chaotic oscillations. The next sub-section offers a brief explanation on the methodology used to calculate the Lyapunov exponents and the Lyapunov dimension in our numerical simulations.

3.1. Maximum Lyapunov exponent and Lyapunov dimension

Let us assume that a reference trajectory $\mathbf{x}_r(t)$ is defined in the phase plane ($\mathbf{q}$, $\dot{\mathbf{q}}$ plane). The evolution of a neighbouring trajectory when an infinitesimal initial perturbation $\delta\mathbf{x}(t_0)$ is applied to it can be used to detect the existence of chaos by calculating the difference of the two trajectories [37]. In the present study, the evolution of the perturbation $\delta\mathbf{x}(t)$ is governed by the following variational equations directly obtained from Eqs. (16):

$$\begin{cases} \dfrac{\mathrm{d}}{\mathrm{d}t}\delta q_j = \delta y_j \\ \dfrac{\mathrm{d}}{\mathrm{d}t}\delta y_j = -2\zeta_j\omega_j\delta y_j - \displaystyle\sum_{i=1}^{\overline{N}} z_{j,i}\delta q_i - \sum_{n=1}^{\overline{N}}\sum_{i=1}^{\overline{N}}\sum_{k=1}^{\overline{N}} z_{j,i,k}\delta q_n(\delta_{k,n}q_i+\delta_{i,n}q_k) - \sum_{n=1}^{\overline{N}}\sum_{i=1}^{\overline{N}}\sum_{k=1}^{\overline{N}}\sum_{l=1}^{\overline{N}} z_{j,i,k,l}\delta q_n(\delta_{i,n}q_kq_l+\delta_{k,n}q_iq_l+\delta_{l,n}q_kq_i), \end{cases} \tag{17}$$

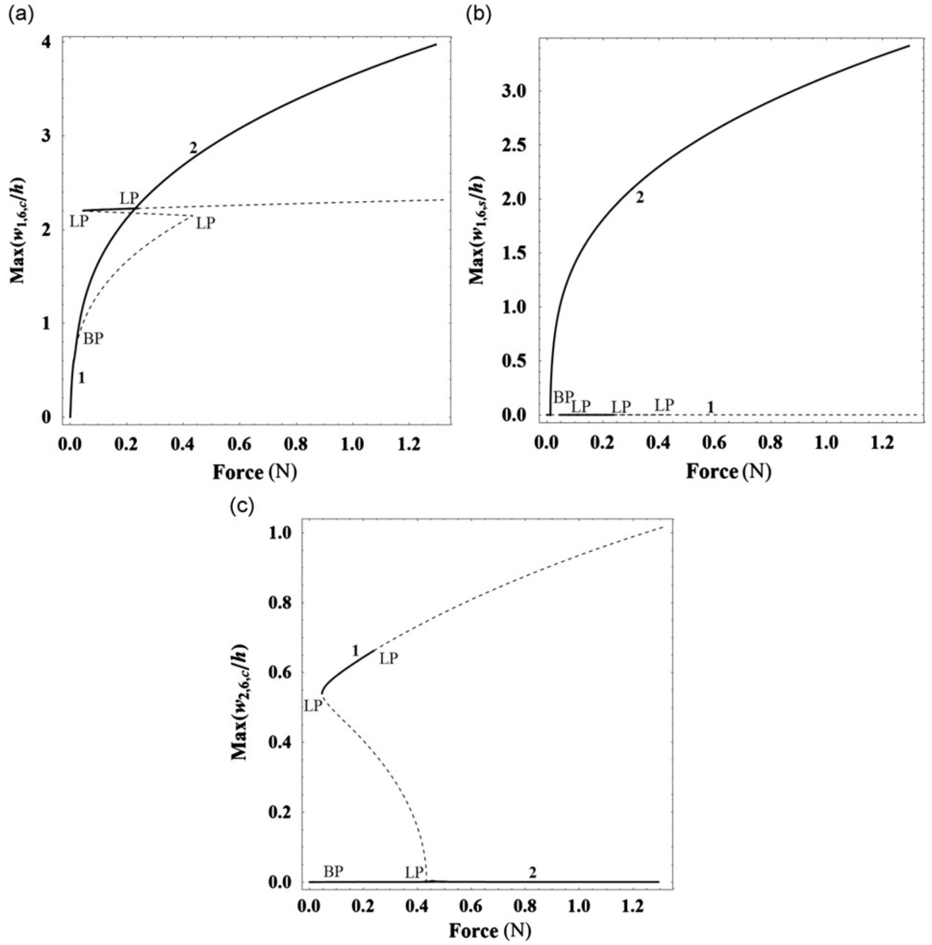

Fig. 5. Shell response for the first asymmetric driven and companion modes and the second asymmetric driven mode as the force amplitude is increased for $\omega/\omega_{1,6}$=1.0 and V=1: ▬▬▬, stable periodic solutions, – – – – –, unstable solutions; (a) first asymmetric driven mode, (b) first asymmetric companion mode, (c) asymmetric driven mode with two longitudinal half-waves. LP denotes limit points, and BP denotes bifurcation points on the diagrams.

where $j = 1, \ldots \overline{N}$, $\delta_{k,n}$ is the Kronecker delta. The numerical integration for Eq. (17) is performed using the DIVPAG Fortran routine; however, the set of equations given in (16) are integrated using an adaptive step-size fourth/fifth order Runge–Kutta method. Steady-state responses are found by ensuring a sufficient number of steps in the numerical integration. For example, to find a reference trajectory, 5×10^6 steps are skipped in order to eliminate the transient in (16) and 1×10^6 steps are skipped to eliminate the transient in the variational Eqs. (17). Then, 1×10^6 steps are used to evaluate the Lyapunov exponent with an initial perturbation of order 1, which is given by

$$\sigma_1 = \limsup_{t \to \infty} \frac{1}{t} \ln|\delta \mathbf{x}(t)|. \tag{18}$$

Then the maximum Lyapunov exponent is calculated by re-normalizing the amplitude of $\delta\mathbf{x}(t)$ using $\delta\overline{\mathbf{x}}(t)_k = \delta\mathbf{x}(t)_k / d_k$, where $|\delta\mathbf{x}(t)|_k = d_k$, at each integration step k, obtaining the following expression:

$$\sigma_{1,k} = \frac{1}{k\Delta t} \sum_{i=1}^{k} \ln d_i. \tag{19}$$

The Fortran computer program developed to calculate $2 \times \overline{N}$ numbers designating the spectrum of the Lyapunov exponents is described and validated in Ref. [38]. In particular, 1×10^7 steps have been used to evaluate the Lyapunov exponents (i.e., 10 times more steps than used in the calculation of the maximum Lyapunov exponents during the numerical integration for the bifurcation diagrams).

To identify the order of chaos in a non-stationary response, a measure of the strangeness of an attractor in the phase-portrait domain must be established by evaluating its fractal dimension. One of the most common fractal dimension indicators is the well-known Lyapunov dimension. The Lyapunov dimension indicates the number of effective independent variables that determines the long-term behaviour of the system. Thus, if the non-stationary response of a deterministic

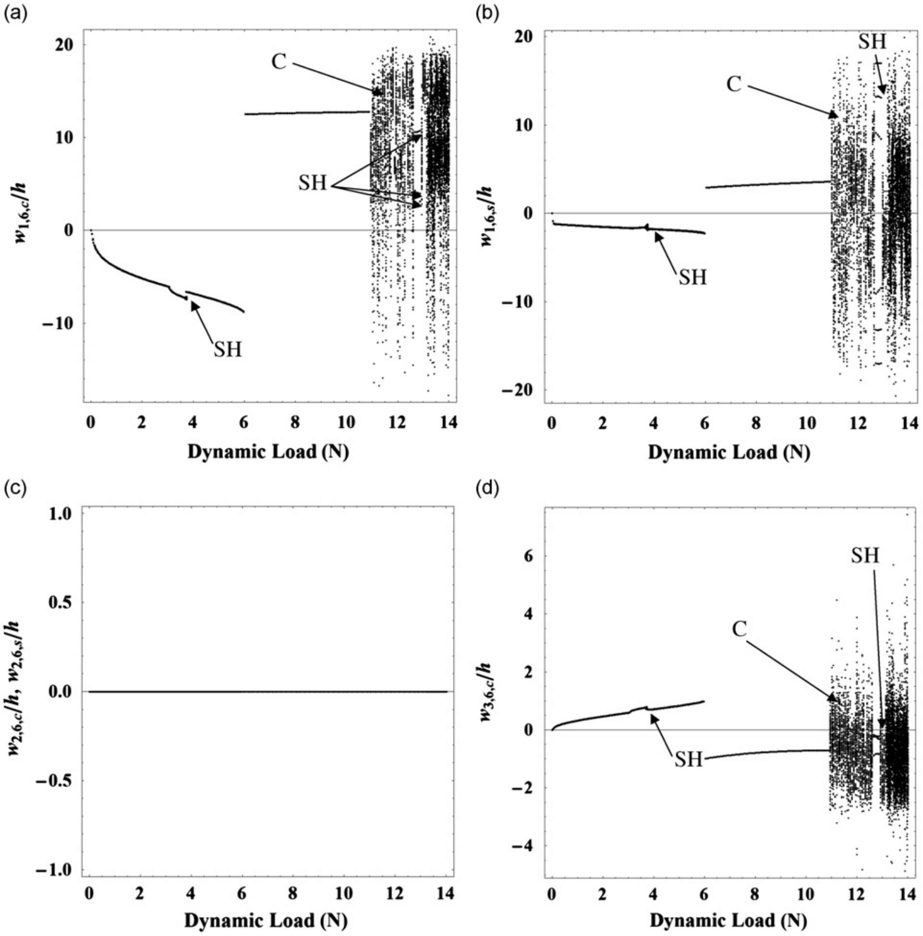

Fig. 6. Bifurcation diagram of Poincaré maps obtained while increasing the force amplitude from 0 to 14.0 N with $\omega/\omega_{1,6}$=1.0 and V=0. (a) Bifurcation diagram for the first driven mode; (b) bifurcation diagram of the first companion mode; (c) bifurcation diagram of the second modes; (d) bifurcation diagram of the third driven mode. SH corresponds to sub-harmonic responses and C denotes chaotic oscillations.

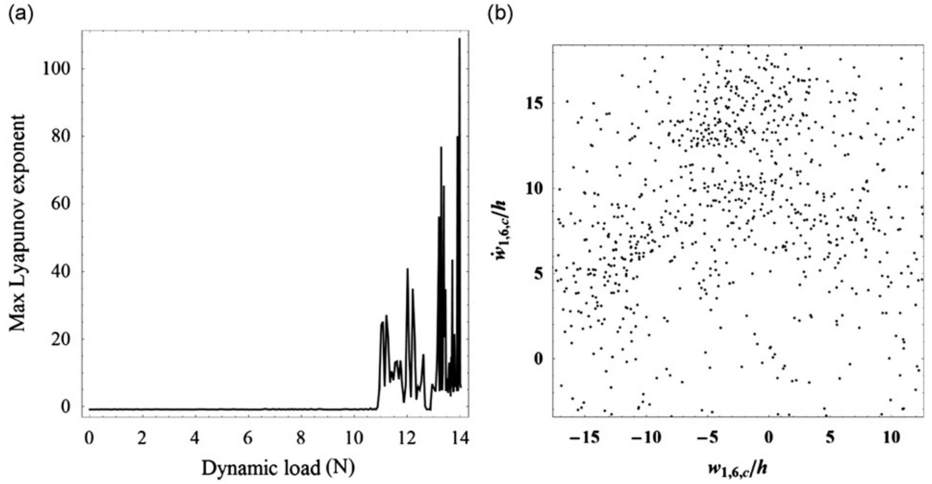

Fig. 7. Maximum Lyapunov exponent and Poincaré maps for the fundamental driven mode when the force is increased to 14.0 N with $\omega/\omega_{1,6}=1.0$ and $V=0$. (a) The maximum Lyapunov exponent; (b) Poincaré map for the fundamental driven mode for $\tilde{f}=12.2$ N.

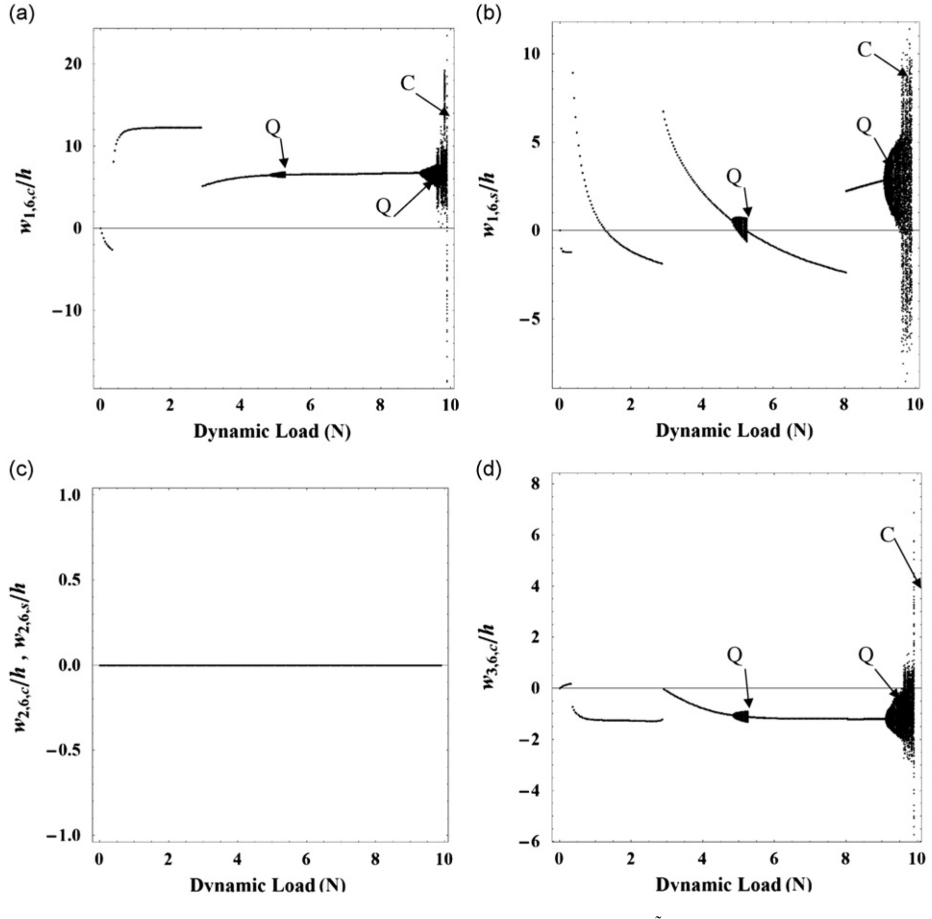

Fig. 8. Bifurcation diagram of Poincaré maps obtained while decreasing the force amplitude from $\tilde{f}=10.0$ to 0 N with $\omega/\omega_{1,6}=1.0$ and $V=0$. Bifurcation diagrams for (a) the first driven mode; (b) the first companion mode; (c) the second modes; (d) the third driven mode. *Q* denotes quasi-periodic responses and *C* chaotic oscillations.

system is characterized by stable or unstable attractors at steady state, then the order of that steady-state response is given by the fractal dimension [26]. The Lyapunov dimension is evaluated from [26]

$$d_L = s + \sum_{r=1}^{s} \sigma_r / |\sigma_{s+1}|, \tag{20}$$

where the Lyapunov exponents are ordered by their magnitude, and s is obtained by satisfying the following conditions:

$$\sum_{r=1}^{s} \sigma_r > 0 \quad \text{and} \quad \sum_{r=1}^{s+1} \sigma_r < 0. \tag{21}$$

4. Numerical results

Numerical calculations are presented for an aluminium shell having the following dimensions and material properties: $L=0.1225$ m, $R=0.041125$ m, $h=0.000137$ m, $\rho_s=2720\,\mathrm{kg/m^3}$, $\nu=0.33$ and $E=70\times10^9$ Pa; such a shell was previously tested experimentally, as described in [21–23]. The assumed stiffness of axial and rotational distributed springs at $x=0$ and L are $k_{a1}=1\times10^7\,\mathrm{N/m^2}$, $k_{a2}=1\times10^5\,\mathrm{N/m^2}$ and $k_r=0.3\times10^3$ N/rad. In the experiments, the shell was glued to solid rings at its two ends with epoxy glue, but the rings were attached to the water tunnel via less stiff silicone glue. Consequently, in the analytical model, the axial springs k_{a1} restraining symmetric modes are taken to be much stiffer than k_{a2} restraining axisymmetric modes. In this way, a boundary condition intermediate between simply supported and clamped ends is obtained. Water is both the contained flowing fluid and the external quiescent liquid, with mass density $\rho_F=1000\,\mathrm{kg/m^3}$. The external quiescent water is confined by a solid cylinder with internal radius of $0.1015\,\mathrm{m} \simeq 2.5R$.

A non-dimensional fluid velocity $V = U/\{(\pi^2/L)[D/(\rho h)]^{1/2}\}$ is introduced for convenience, defined as in [2], where U is the flow velocity and $D = Eh^3/[12(1-\nu^2)]$. For the parameter values given above, the physical flow velocity is obtained by $U=17.12V$. A zero differential pressure, measured at the shell mid-length, is assumed across the shell wall.

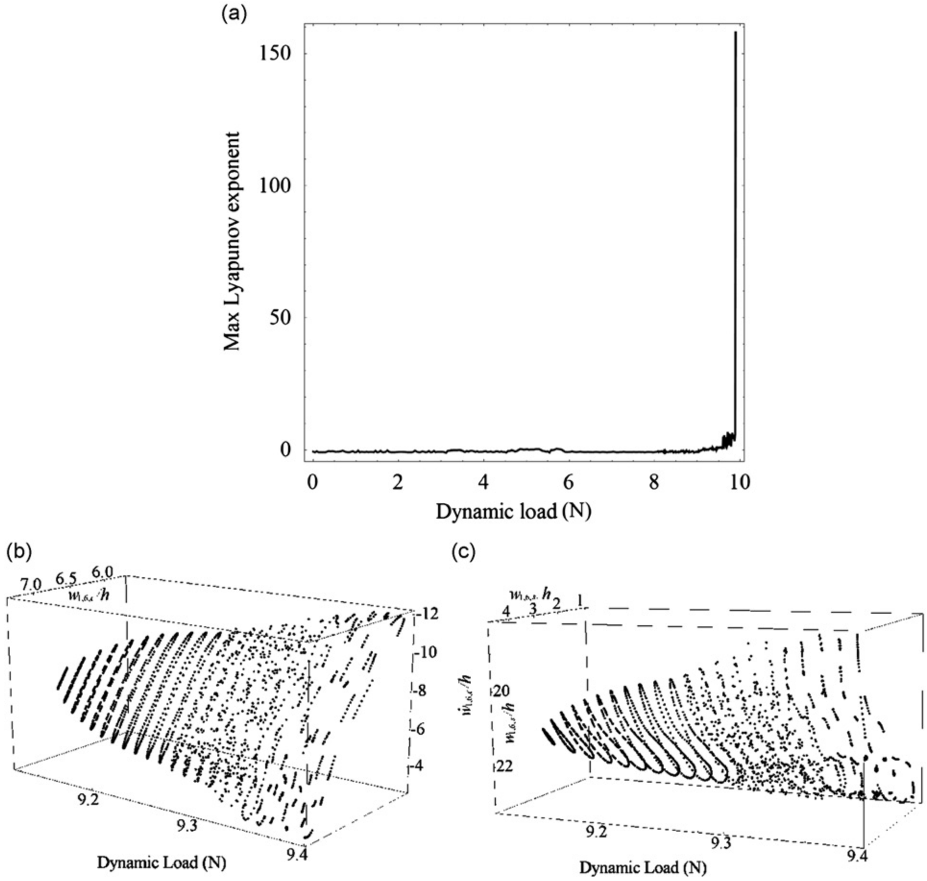

Fig. 9. Maximum Lyapunov exponent and limit cycles when the force is decreased from 10.0 N to zero with $\omega/\omega_{1,6}=1.0$ and $V=0$. (a) The maximum Lyapunov exponent; (b) three-dimensional phase-space plots for different load values for the first driven mode; (c) three-dimensional phase-space plots for different load values for the first companion mode.

The critical circumferential wavenumber observed at divergence in the experiments was $n=6$ [21–23], which is the first mode reaching divergence. Therefore, all the theoretical results presented in this paper are for $n=6$, for which the natural frequency at zero flow velocity ($V=0$) is $\omega_{1,6}=184.6$ Hz. This value decreases with flow; thus, for $V=1$, $\omega_{1,6}=177.85$ Hz, and for $V=2$, $\omega_{1,6}=155.76$ Hz. Moreover, with fluid flow, the vibration modes are no longer the classical natural modes but they become complex. A damping ratio $\zeta_{1,6}=0.005$ is utilized in all the calculations.

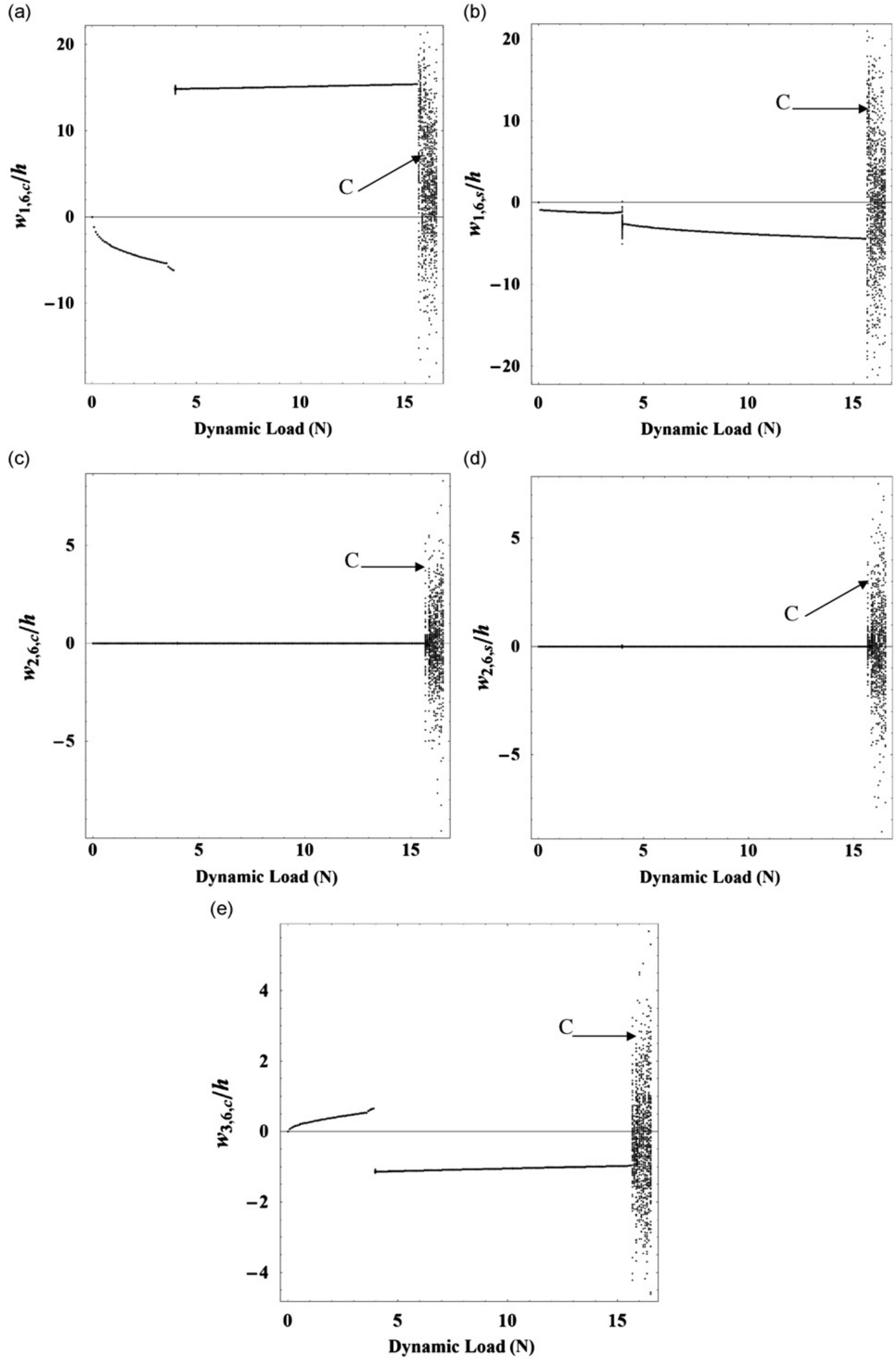

Fig. 10. Bifurcation diagram of Poincaré points for increasing the force amplitude from $\tilde{f}=0$ to 17.0 N with $\omega/\omega_{1,6}=1.0$ and $V=1$. (a) Bifurcation diagram for the driven mode; (b) bifurcation diagram of the companion mode; (c) bifurcation diagram of the second driven mode; (d) bifurcation diagram of the second companion mode; (e) bifurcation diagram of the third driven mode. C denotes the chaotic response of the system.

4.1. Divergence of shell conveying fluid

Fig. 2 is the stability (bifurcation) diagram for the aluminium shell in a plot giving the amplitude of the first generalized coordinate $w_{1,6,c}$ versus the non-dimensional flow velocity, obtained via the AUTO software [36]. As the flow velocity increases, the shell remains undeformed ($w_{1,6,c}$=0) until the pitchfork bifurcation at V=3.69, at which point the system loses stability by static divergence according to linear theory. The solution bifurcates into two unstable branches; these branches fold at V=1.28 and become stable thereafter. As shown for the first time in [15] for simply-supported shells, and later by Karagiozis et al. [22] for clamped shells, there is a range of flow velocities between the point of the linear onset of instability and the folding point in which the shell may jump from its undeformed state to a deformed state of large amplitude if sufficiently perturbed. The perturbation may be in the form of an external force acting on the shell wall or it may be a flow perturbation. In our case, this critical flow range is quite enormous: over 65% of the range ($1.28 \leq V \leq 3.69$) from zero flow velocity to the point of linear loss of stability! It is therefore quite clear that, as perturbations are ubiquitous in real systems, nonlinear analysis must always be performed in the design of such systems for engineering application.

4.2. Frequency–amplitude response

To study the forced response of the aluminium shell, three specific non-dimensional velocities V=0, 1 and 2 have been chosen, corresponding to the points A, B and C, respectively, in the bifurcation diagram Fig. 2. A harmonic point force excitation is applied in the radial direction on the shell surface at $\tilde{x} = L/2$ and $\tilde{\theta} = 0$. Here the forced response is obtained spanning the frequency range around the fundamental resonance. Point A is far short of the range of instability (V=0). The difference between cases B and C is that point B lies before the folding points (LP in Fig. 2), thus only one stable solution on branch 1 exists, namely that of zero shell deformation, while for point C there are at least three stable solutions available (the zero amplitude solution and the two stable branch 2 solutions).

Figs. 3 and 4 show forced reponses for points A, B and C, along with additional cases for different flow velocities, as plots of the non-dimensional vibration amplitude of the shell versus the excitation frequency. The magnitude of the external force was set to a relatively small value: 0.0165 N. In all cases the shell exhibits a softening type of nonlinearity, as expected [18,20], which is more pronounced as the flow velocity is increased. These results were obtained using the AUTO 97 software package.

For case A, see Fig. 3, the excitation frequency is increased gradually and the amplitude of the vibration is increased accordingly following the stable solution branch 1 until it reaches the first limit point (denoted at LP on the plot) and becomes unstable at $\omega/\omega_{1,6} \approx 0.985$. The unstable solution of branch 1 becomes softening and its amplitude increases with decreasing the excitation frequency until it reaches a value very close to the peak vibration amplitude value. For a small region at the peak it becomes stable between $0.977 < \omega/\omega_{1,6} < 0.978$ only to lose stability again right after the peak of the curve and keep decreasing in amplitude with increasing the excitation frequency. At about $\omega/\omega_{1,6} \approx 1.002$ the branch 1 solution loses stability and a new solution branch denoted by number 2 is developed. This pitchfork bifurcation point (BP on the plot) gives rise to unstable solutions for branch 1, where only the driven mode is active (the companion mode is zero). It also gives rise to an initially stable branch 2 with companion mode participation (as shown in Fig. 3(b)). It is interesting to note that the stable branch becomes quiasi-periodic through two Neimark-Sacker (torus) bifurcations at

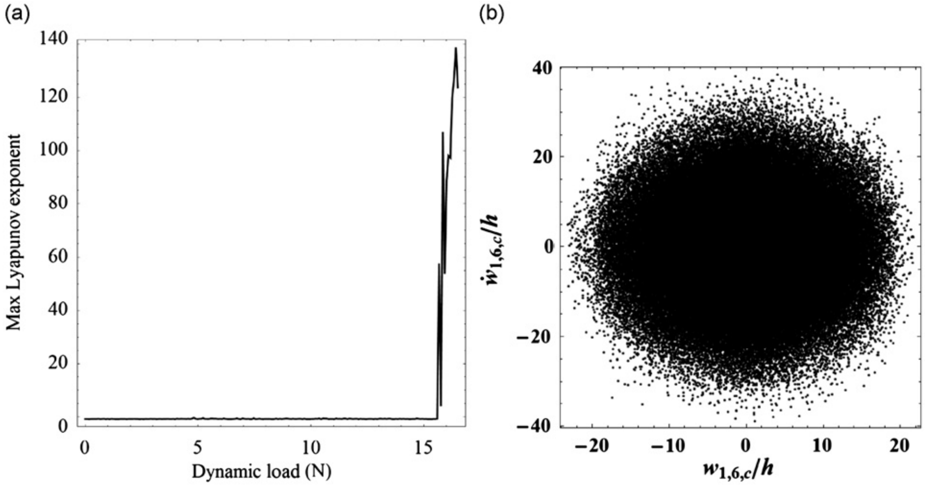

Fig. 11. Maximum Lyapunov exponent and Poincaré maps for the fundamental driven mode when the force $\tilde{f}$ is increased to 17.0 N with $\omega/\omega_{1,6}$=1.0 and V=1. (a) Maximum Lyapunov exponent versus the dynamic load; (b) Poincaré map for the fundamental driven mode for $\tilde{f} = 15.83$ N.

$\omega/\omega_{1,6} = 0.991$ and $\omega/\omega_{1,6} = 0.98039$ (denoted as TR in the figure), therefore the response is quasi-periodic vibrations in the frequency range $0.98039 < \omega/\omega_{1,6} < 0.991$. For excitation frequencies larger than $\omega/\omega_{1,6} = 1.002$ only the stable solution 1 branch of the driven mode is active with zero participation from the companion mode as shown in Fig. 3.

The results for cases B and C are shown in Figs. 4(a, b) and (c, d), respectively. As the flow velocity increases, the region for quasi-periodic responses also increases. It is also noted that, as the flow velocity increases, the quasi-periodic solution branch (branch 2 between the two torus bifurcation points) interferes with the unstable branch 1 (unstable solution between the limit points) allowing for amplitude-modulated responses. In addition, for higher flow velocities the

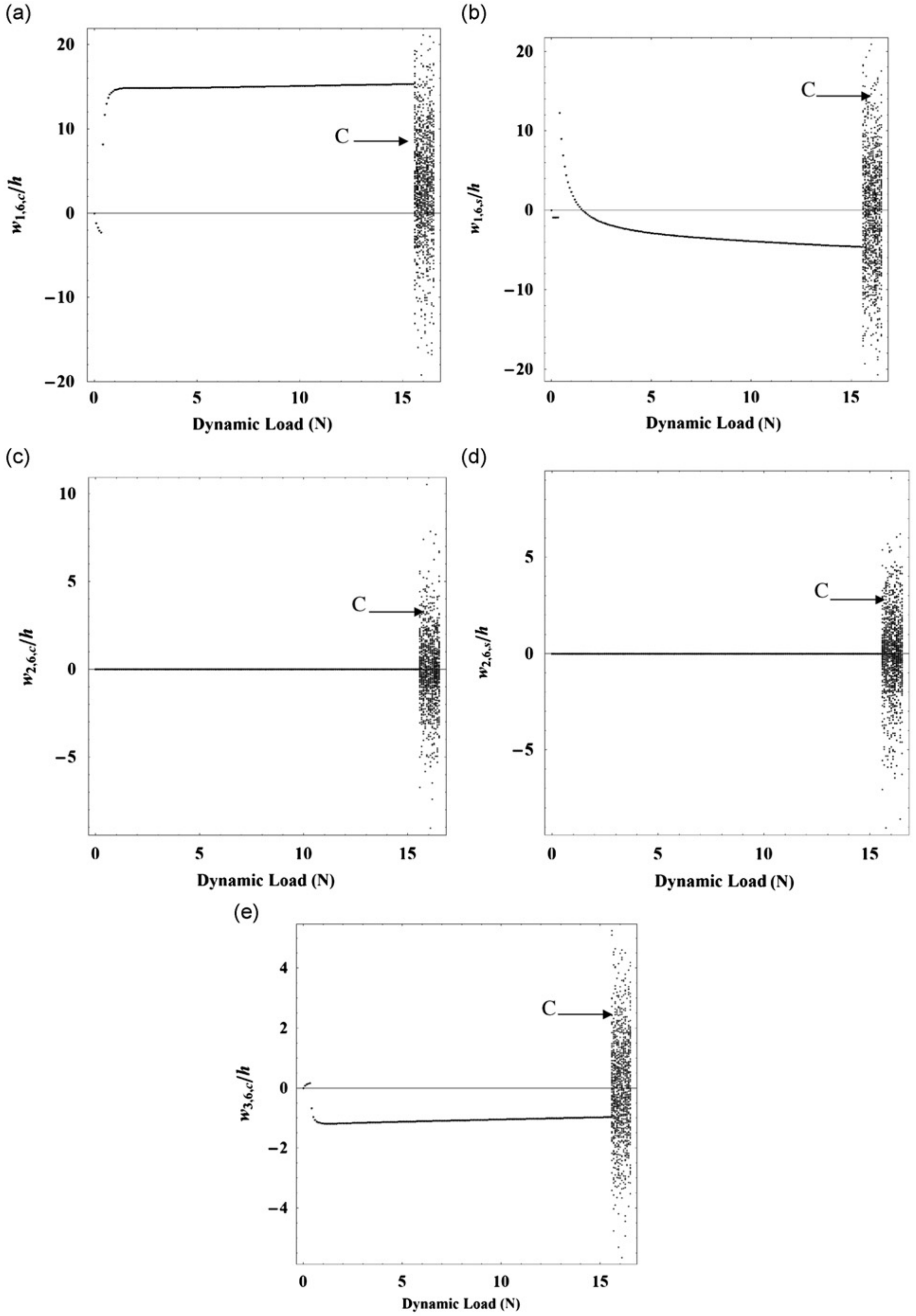

Fig. 12. Bifurcation diagram of Poincaré points for decreasing $\tilde{f}$ from 17.0 to 0 N with $\omega/\omega_{1,6}$=1.0 and V=1. Bifurcation diagrams for (a) the driven mode, (b) the companion mode, (c) the second driven mode, (d) the second companion mode, and (e) the third driven mode. C denotes the chaotic oscillations of the system.

companion mode is activated in a wider range of excitation frequencies. Figs. 4(e) and (f) present frequency–amplitude results for different non-dimensional flow velocities ranging from 0 to 3. The results indicate that for flow velocities smaller than the folding point value (from Fig. 2) the results are almost indistinguishable. However, for higher flow velocities the results exhibit a strong softening behaviour, enhanced by increasing the flow velocity.

4.3. *Force–amplitude response*

In this case, the continuation parameter is the force amplitude, while the frequency is kept constant at resonance. The amplitude of the excitation force $\tilde{f}$ was varied from 0 to 1.32 N for V=1. Fig. 5 summarizes the results for the first asymmetric driven and companion modes and for the second asymmetric driven mode; the non-dimensional amplitude of these modes is plotted versus the amplitude of the excitation force. The results indicate that, as the force reaches a critical value, the system undergoes a pitchfork bifurcation, rendering the solution of branch 1 unstable. A new stable branch 2 solution is generated. If the amplitude of the force is increased further, branch 1 reaches limit point folds and becomes stable exhibiting a strong subcritical behaviour. In Fig. 5(b), it is shown that companion mode participation is activated on branch 2.

It is interesting to see that the effect of the second longitudinal asymmetric mode in the solution is negligible for branch 2; however, it becomes important for a range of force amplitudes on branch 1, as shown in Fig. 5(c).

4.4. *Bifurcation diagrams of Poincaré maps*

In this section, the system dynamics with increasing excitation force is examined via direct numerical integration, thus overcoming the limitations of the AUTO software and being able to see sub-harmonic, quasi-periodic and chaotic responses. Specifically, the DIVPAG Fortran routine was used to integrate the equations of motion, for the three flow velocities corresponding to points A, B and C of Fig. 2, i.e. for V=0, 1 and 2.

It was desired to obtain results with companion mode participation, so that the rich dynamics of the shell could also be captured as a function of time. With the aid of the results from Figs. 3 and 4, and specifically identifying the ranges of frequency when the companion mode participates with non-zero values, six different simulations were conducted with the excitation frequency set at $\omega/\omega_{1,6} = 1.00$. The simulations were done for a non-dimensional force range of 0–14 N (or up to 17 N for case B) with 200 frequency steps; at each step, a Poincaré map and the maximum Lyapunov exponent were calculated. This required a large computational effort, and the computer codes had to be optimized for speed, computational cost and accuracy.

Fig. 6 shows sections of the bifurcation diagram of Poincaré maps for case A (refer to Fig. 2) as plots of the non-dimensional amplitude of the first few modes versus the magnitude of the external force as it was increased from 0 to 14 N.

The results for the first driven mode (Fig. 6(a)) indicate that there is a region of interest between 3.37145 and 3.7610 N in which the period of shell oscillations increases and sub-harmonic responses are observed for $\tilde{f}$ close to 3.761 N (labelled

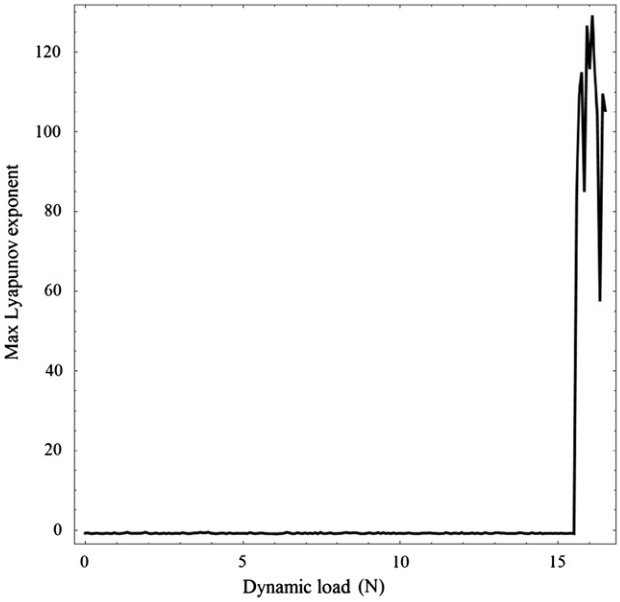

Fig. 13. Maximum Lyapunov exponent versus the dynamic load when the force is decreased from $\tilde{f} = 17.0$ to 0 N with $\omega/\omega_{1,6}$=1.0 and V=1.

as SH in Fig. 6). Another interesting region occurs for $\tilde{f} = 6.03$ N; for this amplitude of $\tilde{f}$ the shell amplitude changes sign: from a negative value to a large positive value. This indicates that there is a change in phase of the response of the system (180°). For $\tilde{f} = 10.9447$ N or higher the shell response is chaotic with some sub-harmonic (SH) windows, as shown in Fig. 6(a). The Lyapunov exponents in the chaotic regions are very large. This is shown in Fig. 7(a), displaying the maximum Lyapunov exponent versus dynamic load. In this case, the second longitudinal asymmetric mode $m=2$ (for both driven and companion modes) is not activated, as shown in Fig. 6(c). However, all other modes are fully activated in the chaotic oscillations. The Lyapunov dimension in this case was calculated to be 55.78 for $\tilde{f} = 12.2$ N, indicating a very large hyperchaos. Fig. 7(b), shows the Poincaré map for this value of $\tilde{f}$.

The hysteresis on the onset and cessation of hyperchaos for case A, depending on whether the dynamic load is increased or decreased during the simulation, can be detected by comparing Figs. 6 and 8. The results in Fig. 8 were obtained for the same system with $V=0$ shown in Fig. 6, but the initial value for the force excitation was set to 10 N and was gradually diminished to zero in small steps. Comparing Figs. 6(a) and 8(a) reveals that there is a hysteresis in the cessation of the chaotic oscillations (chaos appeared when $\tilde{f}=10.9447$ N in Fig. 6 and 9.59 N in Fig. 8). This is an interesting nonlinear result

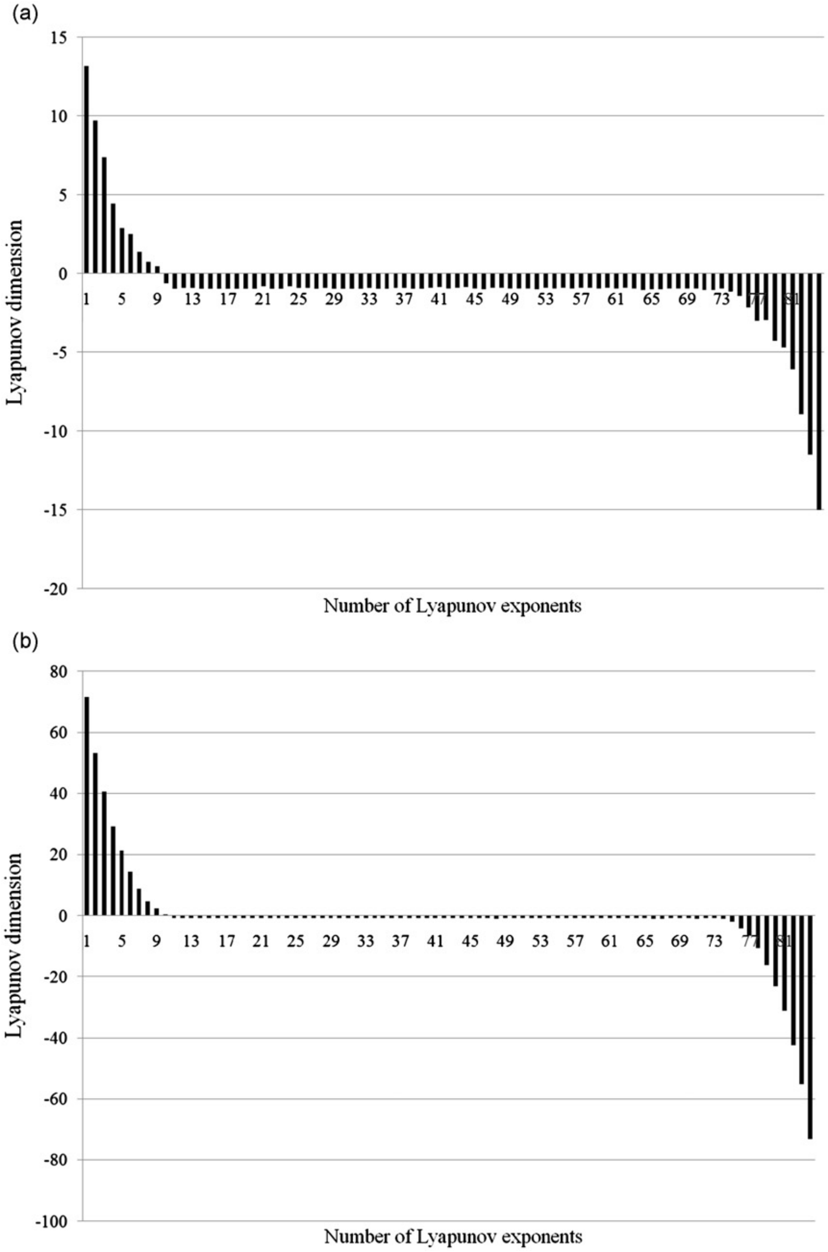

Fig. 14. Plot of all the Lyapunov exponents. (a) Case A with $V=0$ and $\tilde{f} = 12.2$ N; (b) case B when $V=1$ and $\tilde{f} = 15.83$ N.

which emphasizes the complexity of the system when both the driven and companion modes coexist with non-zero amplitudes. Similarly, as in Fig. 6(c), the second asymmetric mode amplitude remains zero throughout the run, as shown in Fig. 8(c). The results in Fig. 8 show a very interesting dynamic system behaviour, with chaotic and sub-harmonic responses along with changes in the phase response of the system as indicated in Figs. 8 and 9(b,c). The maximum Lyapunov exponent is also very large indeed for $\tilde{f} > 9.6$ N, as shown in Fig. 9.

Results for case B (V=1), when $\tilde{f}$ is steadily increased from 0 to 17 N, are shown in Fig. 10. The results in Fig. 10(a) for the first driven mode show that there is a complex periodic response with jumps and phase changes along with sub-harmonic

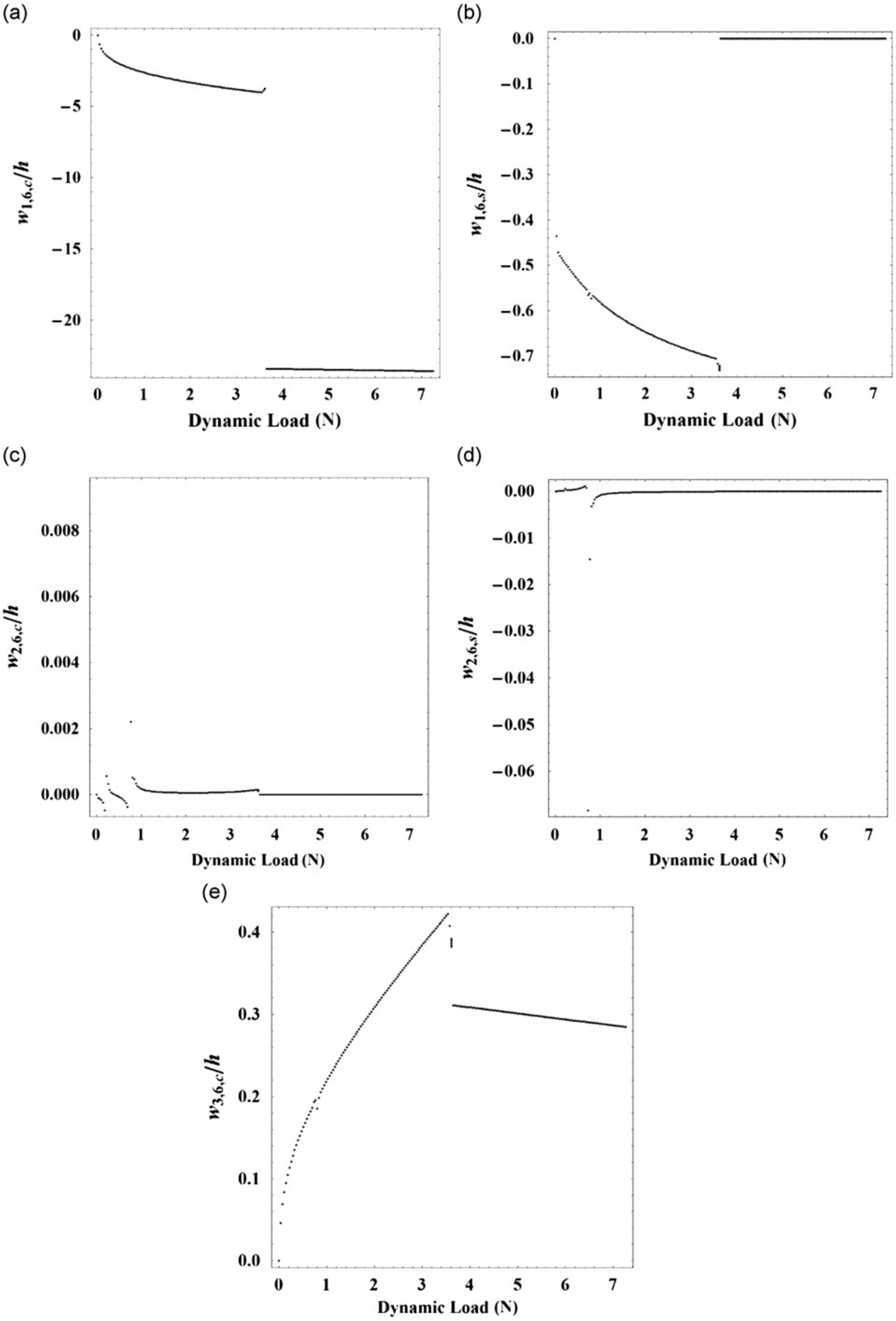

Fig. 15. Bifurcation diagram of Poincaré points for increasing the force amplitude from 0 to 7.26 N with $\omega/\omega_{1,6}$=1.0 and V=2. Bifurcation diagrams for (a) the first driven mode, (b) the first companion mode, (c) the second driven mode, (d) the second companion mode, and (e) the third driven mode.

responses for low excitation values. The first companion mode, shown in Fig. 10(b), goes through similar intervals of sub-harmonic response for low excitation load values. For higher excitation values the system becomes chaotic. In contrast to case A (where $V=0$), here the second asymmetric mode, $w_{2,6,c}(t)$, is activated when the system becomes chaotic; both driven and companion components of the second mode are very active, contributing large displacements when the system experiences chaos. Therefore, the presence of a flowing fluid *vis-à-vis* a quiescent one ($V=0$) is quite important; it amplifies the complexity of the system response.

The chaotic nature of the system can be seen in Fig. 11(a), in a plot of the maximum Lyapunov exponent versus the excitation force magnitude, $\tilde{f}$. Around $\tilde{f}=15.7$ N the Lyapunov exponent becomes very large and positive. The Poincaré map is shown in Fig. 11(b) for $\tilde{f}=15.83$ N.

Once more, as for $V=0$, the hysteresis in the onset of chaotic oscillations was investigated by initializing the system with a dynamic load value of 17 N, and then decreasing it to zero. In Fig. 12(a), the response of the first driven asymmetric mode shows that the chaotic oscillations become simple periodic responses for $f_r<15.05$ N. Looking at Figs. 10(a) and 12(a) and comparing with the results for $V=0$, we can see that the hysteresis in the occurrence and cessation of chaos is smaller than in case of $V=1$. For smaller values of $\tilde{f}$ the system undergoes a change in phase, as indicated in Figs. 12(a) and (b) for the first driven and companion mode components. In this case also, the second asymmetric mode participates in the chaotic oscillations with large amplitude for both the driven and companion modes, as shown in Figs. 12(c) and (d). The maximum Lyapunov exponents, shown in Fig. 13, are again large positive numbers for $\tilde{f}>15.5$; obviously indicating chaotic behaviour.

The Lyapunov spectrum (i.e. all the Lyapunov exponents) for cases A ($V=0$) and B ($V=1$) is shown in Fig. 14. In both cases the Lyapunov dimension is high, thus proving the existence of hyperchaos. For case B the Lyapunov dimension is 82.97 for $\tilde{f}=15.83$ N, indicating that the dimension is larger for the system in the presence of fluid flow.

For case C ($V=2$) the bifurcation diagrams are shown in Fig. 15. The first driven mode is shown in Fig. 15(a). As the load values increase, the system jumps from a small stable response to larger amplitude corresponding to the divergence (buckled) deformation of the shell, as discussed in connection with Fig. 2. It is interesting to note that for a dynamic load $\tilde{f}=3.6$ N the system exhibits sub-harmonic response before jumping to an attractive well solution of very large amplitude. This is true because case C corresponds to a point that lies on the right of the two folding points of branches 2 in the stability results of Fig. 2. Therefore, the attractiveness of the two stable branches (branches 2 in Fig. 2) is large and they capture the shell vibration for $\tilde{f}=3.648$ N. This is different from the behaviour for flow velocity values that are smaller than the folding point velocities shown in Fig. 2. The first companion mode also exhibits the complicated sub-harmonic responses for lower force values, but it becomes zero at divergence. The second mode behaviour is also complicated, as shown in Fig. 15(c) and (d). The sub-harmonic response is clearly present; however, the response becomes more complicated with additional jumps. The response of the third driven mode, shown in Fig. 15(e), is also complicated.

The quasi-periodic regions indicated in Fig. 15(a) can also be seen in the maximum Lyapunov exponent diagram in Fig. 16. The spikes at smaller load values and in the region $3.6<\tilde{f}<3.648$ N indicate the quasi-periodic regions. However,

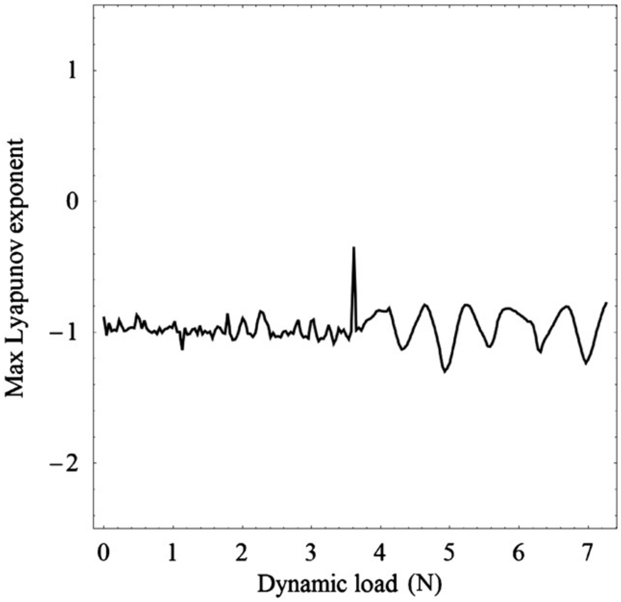

Fig. 16. The maximum Lyapunov exponent versus the dynamic load values for $V=2$ (case C) with $\omega/\omega_{1,6}=1.0$ when the force amplitude is increased from zero to $\tilde{f}=7.26$ N.

no chaotic oscillations can be observed for the investigated value of the excitation force. It is important to observe that once buckling of the shell is reached at $\tilde{f}=3.648\,\text{N}$, just periodic responses are observed. In order to observe chaotic response, it is necessary to reach values for $\tilde{f}$ close to 100 N, i.e. a very large force is necessary to have chaotic vibrations of the buckled shell. In fact, the buckled shell is stiffer than the undeformed shell, so that it has a natural frequency higher than $\omega_{1,n}$ and therefore it is away from resonance for excitation frequency $\omega/\omega_{1,6}=1.00$.

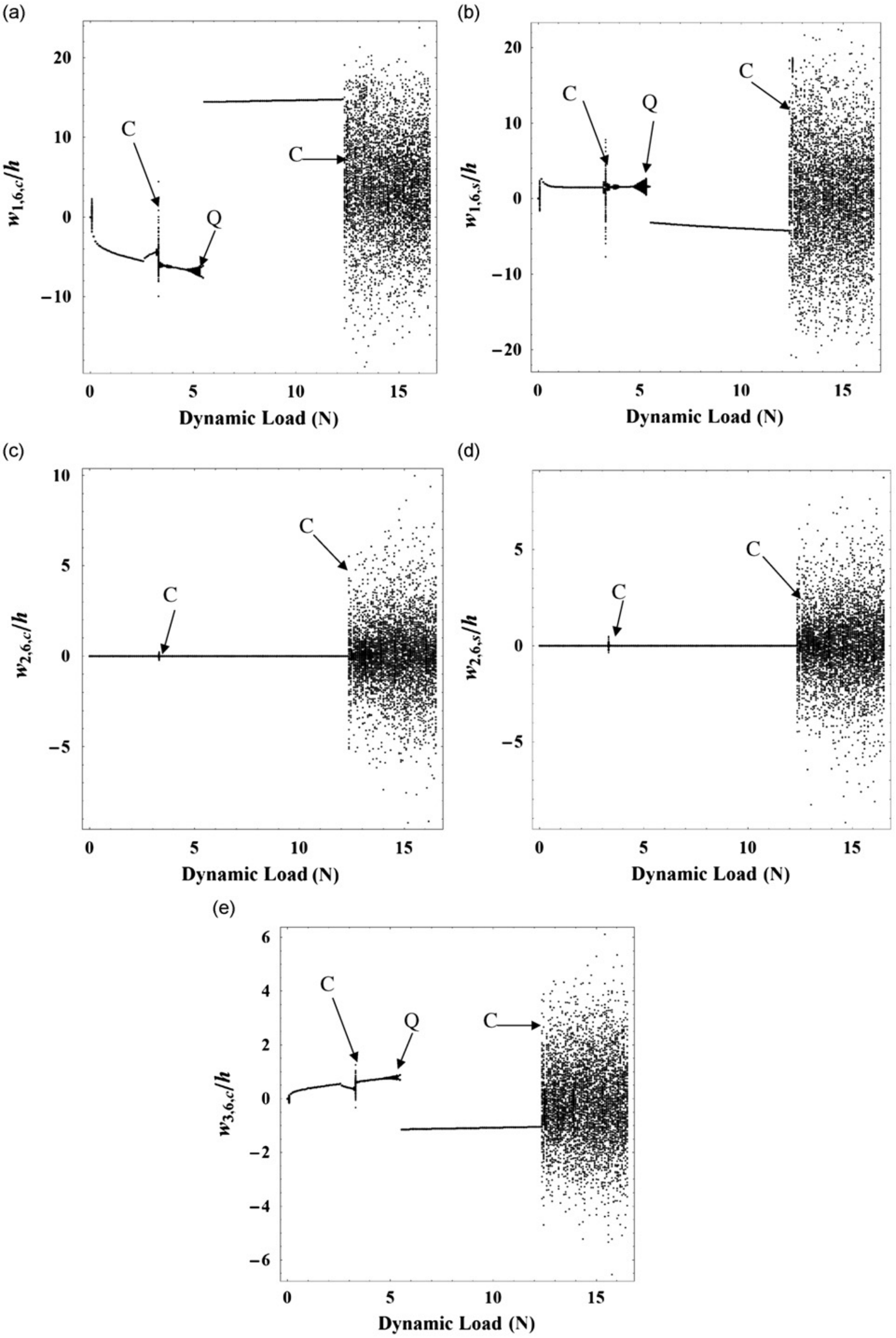

Fig. 17. Bifurcation diagram of Poincaré points for increasing the force amplitude from 0 to 17.0 N with $\omega/\omega_{1,6}=0.95$ and $V=1$. Bifurcation diagrams for (a) the first driven mode, (b) the second companion mode, (c) the second driven mode, (d) the second companion mode, and (e) the third driven mode. Q denotes the quasi-periodic response of the system and C the chaotic oscillations of the shell.

Additional calculations for the same system with a flow velocity $V=1$ and excitation frequency equal to $\omega/\omega_{1,6}=0.95$ are shown in Fig. 17. It is evident that the system undergoes complicated changes in its response in this case, involving periodic, sub-harmonic, quasi-periodic and chaotic oscillations. In this case also, the second mode (when $m=2$ for the driven and companion modes) makes a large contribution to the total displacement when the system is chaotic. In contrast to the cases with $\omega/\omega_{1,6}=1.00$, here chaos appears also for smaller dynamic force values. This is verified in the maximum Lyapunov exponent plot in Fig. 18, where the exponents become large positive numbers even for smaller force values. The complicated response is better shown in Fig. 19 where the first driven mode is plotted as a three-dimensional bifurcation diagram. Finally, in Fig. 20 the complicated sub-harmonic and chaotic response of the first driven mode is shown for different load values.

5. Conclusions

In this paper the complex nonlinear dynamic behaviour of shells conveying fluid under external radial harmonic excitation is investigated. It is shown that a shell conveying fluid can display periodic, quasi-periodic and chaotic responses, depending on the flow velocity, amplitude and frequency of the harmonic excitation. However, if the flow

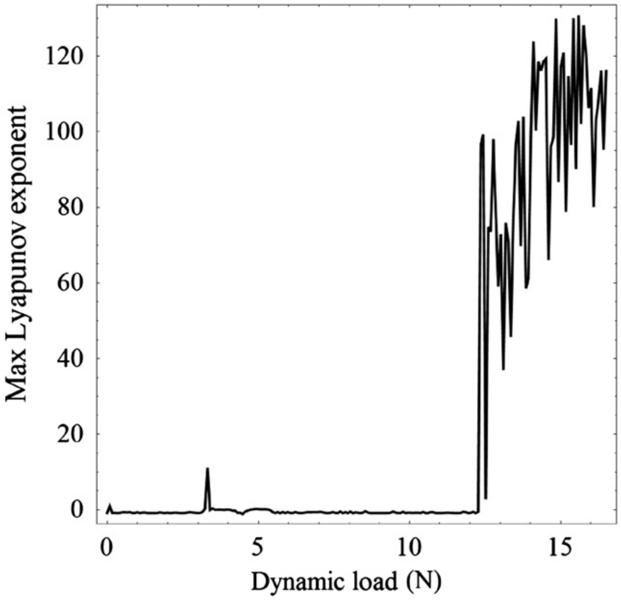

Fig. 18. The maximum Lyapunov exponent versus the dynamic load values for $V=1$ $\omega/\omega_{1,6}=0.95$ when the force amplitude is increased from zero to $\tilde{f}=17.0\,\mathrm{N}$.

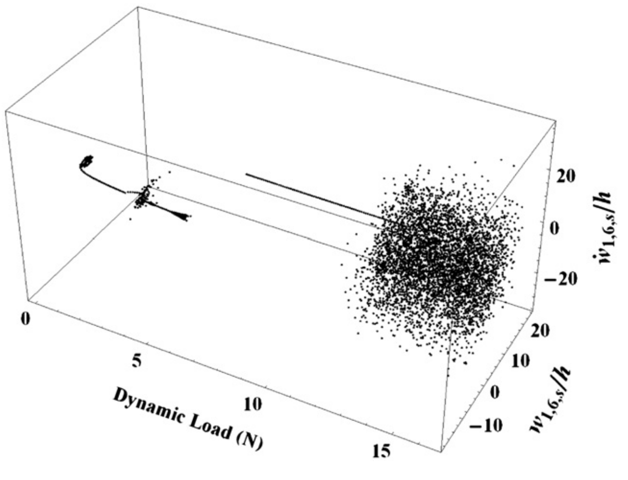

Fig. 19. Three-dimensional response diagram for the first driven mode results, for each increment of the dynamic load for $V=1$ and $\omega/\omega_{1,6}=0.95$.

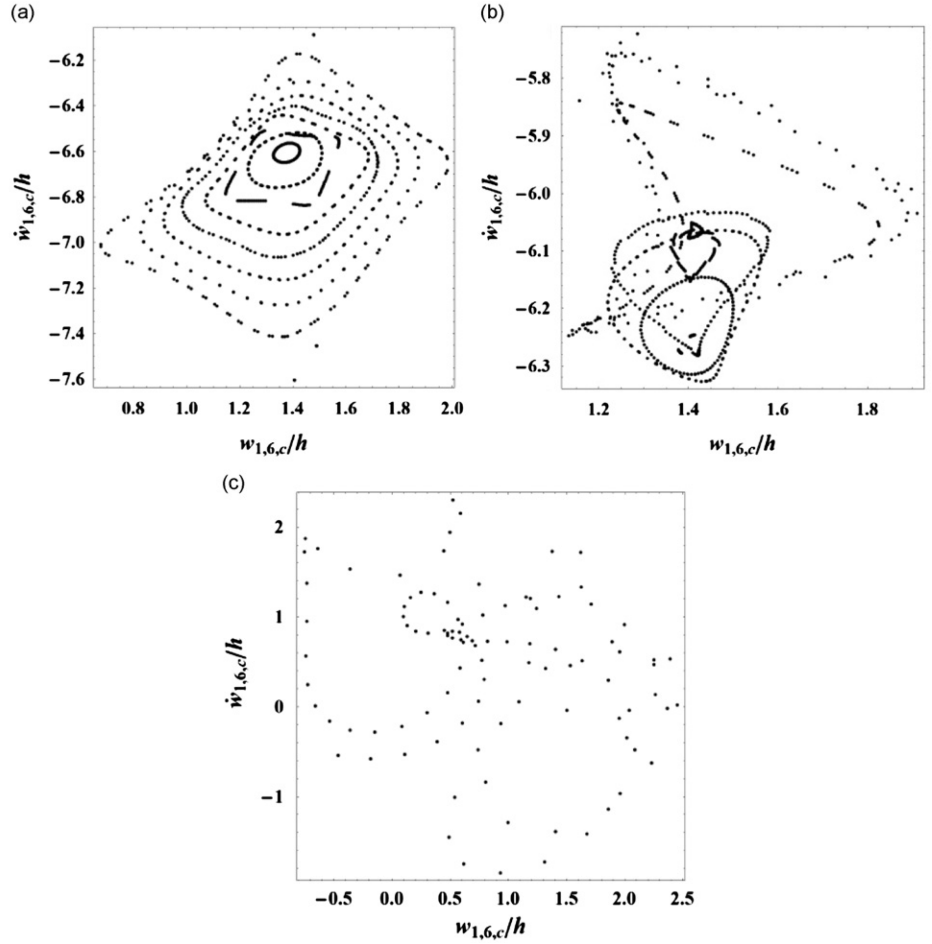

Fig. 20. Phase-space plot for the first driven mode, showing complicated responses for different dynamic load values. (a) First driven mode for dynamic load values $4.726<\tilde{f}<5.4726$ N; (b) multi-periodic response for $\tilde{f}=3.399$ to 3.979 N; (c) chaotic response for $\tilde{f}=0.0829$ to 0.65829 N.

velocity is higher than the folding points detected in the stability diagram (V=1.28 in the case investigated numerically), then the harmonically excited shell will easily jump to the bifurcated solution, and in the particular case studied this occurs without any chaotic behaviour; however, sub-harmonic responses are observed before the jump. On the other hand, once the shell is buckled, chaotic nonlinear dynamics can arise, but this occurs only for very large excitations.

For flow velocities below the folding point in the stability diagram, the shell exhibits hysteretic chaotic behaviour; i.e. reducing the excitation force, chaos is obtained for smaller excitations than when increasing the excitation force. It is also shown that the second asymmetric mode (m=2) is important since it actively participates in the hyperchaotic oscillations, contributing to shell deformation with large amplitudes in both the driven and companion modes. Thus, the response is substantially different in the presence of flow in the shell.

Acknowledgements

The authors would like to thank the NSERC Discovery Grant program, Canada Research Chair and Canada Foundation for innovation programs for their financial support, as well as McGill University for a start-up grant.

References

[1] M.P. Païdoussis, J.P. Denise, Flutter of thin cylindrical shells conveying fluid, *Journal of Sound and Vibration* 20 (1972) 9–26.
[2] D.S. Weaver, T.E. Unny, On the dynamic stability of fluid-conveying pipes, *Journal of Applied Mechanics* 40 (1973) 48–52.
[3] M.P. Païdoussis, S.P. Chan, A.K. Misra, Dynamics and stability of coaxial cylindrical shells containing flowing fluid, *Journal of Sound and Vibration* 97 (1984) 201–235.
[4] M.P. Païdoussis, *Fluid–Structure Interactions: Slender Structures and Axial Flow*, Vol. 2, Elsevier Academic Press, London, UK, 2003.

[5] J. Horàček, I. Zolotarev, Influence of fixing edges of a cylindrical shell with conveying fluid on its dynamic characteristics, *Soviet Applied Mechanics* 20 (1984) 756–765.
[6] M. Amabili, R. Garziera, Vibrations of circular cylindrical shells with nonuniform constraints, elastic bed and added mass; part II: shells containing or immersed in axial flow, *Journal of Fluids and Structures* 16 (2002) 31–51.
[7] M. Amabili, R. Garziera, Vibrations of circular cylindrical shells with nonuniform constraints, elastic bed and added mass; part III: steady viscous effects on shells conveying fluid, *Journal of Fluids and Structures* 16 (2002) 795–809.
[8] B. Ugurlu, A. Ergin, A hydroelastic investigation of circular cylindrical shells-containing flowing fluid with different end conditions, *Journal of Sound and Vibration* 318 (2008) 1291–1312.
[9] M.H. Toorani, A.A. Lakis, Shear deformations in dynamic analysis of anisotropic laminated open cylindrical shells filled with or subjected to a flowing fluid, *Computer Methods in Applied Mechanics and Engineering* 190 (2001) 4929–4966.
[10] M.H. Toorani, A.A. Lakis, Dynamic analysis of anisotropic cylindrical shells containing flowing fluid, *Journal of Pressure Vessel Technology* 123 (2001) 454–460.
[11] M.H. Toorani, A.A. Lakis, Dynamic behavior of axisymmetric and beam-like anisotropic cylindrical shells conveying fluid, *Journal of Sound and Vibration* 259 (2003) 265–298.
[12] Y.L. Zhang, J.M. Reese, D.G. Gorman, Finite element analysis of the vibratory characteristics of cylindrical shells conveying fluid, *Computer Methods in Applied Mechanics and Engineering* 191 (2002) 5207–5231.
[13] Y.L. Zhang, J.M. Reese, D.G. Gorman, A comparative study of axisymmetric finite elements for the vibration of thin cylindrical shells conveying fluid, *International Journal for Numerical Methods in Engineering* 54 (2002) 89–110.
[14] A. Selmane, A.A. Lakis, Non-linear dynamic analysis of orthotropic open cylindrical shells subjected to a flowing fluid, *Journal of Sound and Vibration* 202 (1997) 67–93.
[15] M. Amabili, F. Pellicano, M.P. Païdoussis, Non-linear dynamics and stability of circular cylindrical shells containing flowing fluid. Part I: stability, *Journal of Sound and Vibration* 225 (1999) 655–699.
[16] M. Amabili, F. Pellicano, M.P. Païdoussis, Non-linear dynamics and stability of circular cylindrical shells containing flowing fluid, part II: large-amplitude vibrations without flow, *Journal of Sound and Vibration* 228 (1999) 1103–1124.
[17] M. Amabili, F. Pellicano, M.P. Païdoussis, Non-linear dynamics and stability of circular cylindrical shells containing flowing fluid. Part III: truncation effect without flow and experiments, *Journal of Sound and Vibration* 237 (2000) 617–640.
[18] M. Amabili, F. Pellicano, M.P. Païdoussis, Non-linear dynamics and stability of circular cylindrical shells containing flowing fluid. Part IV: large-amplitude vibrations with flow, *Journal of Sound and Vibration* 237 (2000) 641–666.
[19] M. Amabili, F. Pellicano, M.P. Païdoussis, Nonlinear stability of circular cylindrical shells in annular and unbounded axial flow, *Journal of Applied Mechanics* 68 (2001) 827–834.
[20] M. Amabili, F. Pellicano, M.P. Païdoussis, Non-linear dynamics and stability of circular cylindrical shells conveying flowing fluid, *Computers and Structures* 80 (2002) 899–906.
[21] K.N. Karagiozis, M.P. Païdoussis, A.K. Misra, E. Grinevich, An experimental study of the nonlinear dynamics of cylindrical shells with clamped ends subjected to axial flow, *Journal of Fluids and Structures* 20 (2005) 801–816.
[22] K.N. Karagiozis, M.P. Païdoussis, M. Amabili, A.K. Misra, Nonlinear stability of cylindrical shells subjected to axial flow: theory and experiments, *Journal of Sound and Vibration* 309 (2008) 637–676.
[23] M. Amabili, K. Karagiozis, M.P. Païdoussis, Effect of geometric imperfections on nonlinear stability of circular cylindrical shells conveying fluid, *International Journal of Non-Linear Mechanics* 44 (2009) 276–289.
[24] M. Bathe, R.D. Kamm, Fluid–structure interaction analysis in biomechanics, *Proceedings of the First MIT Conference on Computational Fluid and Solid Mechanics*, Cambridge, MA, USA, Vol. 2, 2003, pp. 1068–1072.
[25] M. Amabili, M.P. Païdoussis, Review of studies on geometrically nonlinear vibrations and dynamics of circular cylindrical shells and panels, with and without fluid–structure interaction, *Applied Mechanics Reviews* 56 (2003) 349–381.
[26] M. Amabili, *Nonlinear Vibrations and Stability of Shells and Plates*, Cambridge University Press, New York, USA, 2008.
[27] M. Amabili, Theory and experiments for large-amplitude vibrations of empty and fluid-filled circular cylindrical shells with imperfections, *Journal of Sound and Vibration* 262 (2003) 921–975.
[28] M. Amabili, Comparison of shell theories for large-amplitude vibrations of circular cylindrical shells: Lagrangian approach, *Journal of Sound and Vibration* 264 (2003) 1091–1125.
[29] M.S. Soliman, P.B. Gonçalves, Chaotic behavior resulting in transient and steady state instabilities of pressure-loaded shallow spherical shells, *Journal of Sound and Vibration* 259 (2003) 497–512.
[30] M. Amabili, A. Sarkar, M.P. Païdoussis, Chaotic vibrations of circular cylindrical shells: Galerkin versus reduced-order models via the proper orthogonal decomposition method, *Journal of Sound and Vibration* 290 (2006) 736–762.
[31] K. Forsberg, Influence of boundary conditions on the modal characteristics of thin cylindrical shells, *AIAA Journal* 2 (1964) 2150–2157.
[32] P.B. Gonçalves, R.C. Batista, Non-linear vibration analysis of fluid-filled cylindrical shells, *Journal of Sound and Vibration* 127 (1988) 133–143.
[33] A.A. Lakis, A. Laveau, Non-linear dynamic analysis of anisotropic cylindrical shells containing a flowing fluid, *International Journal of Solids and Structures* 28 (1991) 1079–1094.
[34] A. Selmane, A.A. Lakis, Non-linear dynamic analysis of orthotropic open cylindrical shells subjected to a flowing fluid, *Journal of Sound and Vibration* 202 (1997) 67–93.
[35] M.P. Païdoussis, A.K. Misra, S.P. Chan, Dynamics and stability of coaxial cylindrical shells conveying viscous fluid, *Journal of Applied Mechanics* 52 (1985) 389–396.
[36] E.J. Doedel, A.R. Champneys, T.F. Fairgrieve, Y.A. Kuznetsov, B. Sandstede, X. Wang, *AUTO 97: Continuation and Bifurcation Software for Ordinary Differential Equations (with HomCont)*, Concordia University, Montreal, Canada, 1998.
[37] J. Argyris, G. Faust, H. Haase, *An Exploration of Chaos*, North-Holland, Amsterdam, 1994.
[38] M. Amabili, Non-linear vibrations of doubly curved shallow shells, *International Journal of Non-Linear Mechanics* 40 (2005) 683–710.